J. Fluid Mech. (1999), *vol.* 383, *pp.* 75–112. Printed in the United Kingdom

Large-eddy simulation of flow over wavy surfaces

By DOUGLAS S. HENN and R. IAN SYKES

ARAP Group/Titan Research & Technology, Princeton, NJ 08543-2229, USA

(Received 23 March 1998 and in revised form 7th October 1998)

Large-eddy simulation is used to investigate fully developed turbulent flow in a neutral channel wherein the lower wall is sinusoidal. The numerical results are compared with experimental observations for wave slopes ranging from 0 to 0.628. Particular emphasis is placed on the separated flow induced by a large-amplitude wave. A detailed comparison with the data of Buckles, Hanratty & Adrian (1984) shows generally good agreement. Large-eddy simulation surface pressures are integrated to calculate form drag as a function of wave slope. Drag is found to increase quadratically with slope for small-amplitude waves, with a somewhat slower increase for larger amplitudes. However, comparison with experimental measurements is confounded by uncertainties with the values reported in the literature. An interesting feature characteristic of all wavy-surface simulations is an increase in transverse velocity fluctuations on the wave upslope. Although the precise mechanism responsible is not known, analysis shows it to be associated with temporally persistent vortex-like structures localized near the surface. The magnitude of the fluctuation increase appears to scale quadratically with slope for small-amplitude waves, in contrast to the streamwise fluctuations, which increase linearly.

1. Introduction

The use of large-eddy simulations to model complex flow configurations is becoming increasingly common. One of the earliest applications to go beyond the horizontally homogeneous channel case was in modelling turbulent convective flow over sinusoidal terrain, e.g. Krettenauer & Schumann (1992); Walko, Cotton & Pielke (1992); and Dörnbrack & Schumann (1993). Simulations over flat homogeneous terrain have demonstrated that this type of flow is particularly amenable to large-eddy simulation (LES) since the dominant thermally-driven eddies are on the scale of the mixed-layer height (or channel depth) and so are typically well-resolved (Mason 1989; Schmidt & Schumann 1989). While LES has shown that wavy terrain can modify the large-scale flow in the convective boundary layer, horizontally averaged profiles are not very different from the flat case, even in the presence of a mean wind. This is because strong vertical mixing tends to reduce the velocity shears caused by even large surface slopes. However, the effects of terrain on more neutrally stable flow are likely to be much more dramatic since even relatively small slopes can induce significant variations in the mean flow and turbulence structure (Taylor 1977; Sykes 1980; Belcher & Hunt 1998).

This research effort is oriented towards atmospheric flow over terrain which, while idealized, is nonetheless realistic in terms of slope and wavelength. However, before making this extension, it is desirable to verify the LES against laboratory measurements. Gong, Taylor & Dörnbrack (1996) recently presented experimental observations and LES calculations for wind-tunnel flow over sinusoidal terrain with a growing boundary layer. However, the flow is complicated by the non-uniformity of the boundary layer and may also be influenced by the lateral walls of the wind tunnel. Hanratty and coworkers have presented an extensive set of measurements of channel flow over wavy surfaces (e.g. Zilker, Cook & Hanratty 1977; Zilker & Hanratty 1979; Buckles, Hanratty & Adrian 1984 (hereinafter referred to as BHA), 1986; Frederick & Hanratty 1988; Kuzan, Hanratty & Adrian 1989; Hudson, Dykhno & Hanratty 1996). We will focus in particular on the data of BHA, who present extensive measurements of the mean and fluctuating velocity for turbulent channel flow over an aerodynamically smooth, large-amplitude sinusoidal surface. However, we will also consider smaller-amplitude waves in order to establish confidence in the model as well as examine the effects of varying wave slope. Although the data we are comparing with are all for smooth walls and hence Reynolds-number dependent, the Reynolds numbers are high enough so that the flows are fully turbulent. Nonetheless, the LES model does account for finite-Reynolds-number effects since a no-slip velocity boundary condition is used.

Analytic flow studies (e.g. Sykes 1980; Hunt, Leibovich & Richards 1988; Belcher, Newley & Hunt 1993), have shown that terrain-induced turbulence modifications are subject to rapid variation close to the surface. The equilibrium log-layer relations are valid only very near the boundary, and an inner layer develops in which advection and distortion of the turbulence are important, with a vertical scale much smaller than the horizontal wavelength. The inner layer is typically about 5% of the wavelength, making explicit resolution of eddies in this region very difficult. These difficulties also affect the ability to represent surface forces correctly, since the forces are closely coupled to the details of the flow near the boundary. However, the total drag force is also related to the total energy dissipation in the flow, and we expect wavy surfaces, especially in the case of large-scale separation, to generate resolvable eddies well suited to modelling by LES.

Direct numerical simulations of channel flow over wavy surfaces (e.g. Maaß & Schumann 1994, 1996; De Angelis, Lombardi & Banerjee 1997; Cherukat *et al.* 1998) have successfully reproduced many of the laboratory observations for moderate Reynolds number, while also providing great detail on the flow structure. For instance, both De Angelis *et al.* and Cherukat *et al.* note increased transverse fluctuations on the wave upslope, which we have observed for a range of wave amplitudes. However, the application of DNS is limited since resolution requirements become prohibitive for high-Reynolds-number flow.

The paper is organized as follows. First, the LES model is described, with particular emphasis on features relevant to finite-Reynolds-number flow over wavy surfaces, since the infinite Reynolds number, Cartesian version of the model has been described elsewhere. The numerical methods and boundary conditions are then briefly outlined. After summarizing the basic flow configurations and parameters, model results are compared with a number of experiments. We first present results from flat-channel calculations and then proceed to examine a small-amplitude wavy-surface case. Next, LES results are compared in detail with the data of BHA for separated flow over a large-amplitude wave. A limited comparison between flows over waves with different amplitudes is then made; the dependence of form drag on wave slope is examined in particular. Finally, the interesting feature of increased transverse turbulent fluctuations on the wave upslope is investigated.

2. LES model

2.1. *Model equations*

The basic LES model has previously been applied to buoyancy-driven turbulence (Sykes & Henn 1989; Henn & Sykes 1992) and a neutral boundary layer (Sykes & Henn 1992). For the current application, the terrain-following coordinate transformation of Clark (1977) is used for accurate representation of the surface boundary conditions. The equations of motions are based on the filtered Navier–Stokes equations and follow the approach of Moin & Kim (1982) in explicitly including viscosity so that a no-slip boundary may be imposed. The resolved-scale Cartesian velocity components $u_i = (u, v, w)$ are solved as functions of transformed coordinates $\tilde{x}_i = (\tilde{x}, \tilde{y}, \tilde{z})$, defined in terms of Cartesian coordinates $x_i = (x, y, z)$ by $\tilde{x} = x$, $\tilde{y} = y$ and $\tilde{z} = \eta(x, y, z)$. The transformation

$$\eta = (z - h)/J, \tag{1}$$

where $J = 1 - h/H$, maps the domain between the lower wavy surface at $z = h$ and the upper flat channel wall at $z = H$ onto a rectangular domain. The lower surface is a two-dimensional infinite wavetrain defined by $h(x, y) = a[1 + \cos(2\pi x/\lambda)]$, with wavelength λ and amplitude a.

Cartesian derivatives for an arbitrary scalar field ϕ are given in terms of the transformed coordinates as

$$\frac{\partial}{\partial x_i}\phi = \frac{\partial \tilde{x}_j}{\partial x_i}\frac{\partial}{\partial \tilde{x}_j}\phi \equiv G^{ji}\frac{\partial}{\partial \tilde{x}_j}\phi, \tag{2}$$

where the summation convention is assumed. Note that $J^{-1} = \det(G^{ij})$. Since a fluid of constant density ρ is considered here, it is convenient to define $V = \rho J$. Then, following Krettenauer & Schumann (1992), the model equations are given concisely as

$$\frac{\partial}{\partial \tilde{x}_i}\left(V G^{ij} u_j\right) = 0, \tag{3}$$

$$\frac{\partial}{\partial t}(V u_i) + \frac{\partial}{\partial \tilde{x}_j}\left(V G^{jk} u_k u_i\right) = -\frac{\partial}{\partial \tilde{x}_j}\left(V G^{ji} p\right) + \frac{\partial}{\partial \tilde{x}_j}\left(V G^{jk} \tau_{ik}\right) + \nu \frac{\partial}{\partial \tilde{x}_j}\left(V G^{jk} D_{ik}\right) + V P_x \delta_{1i}, \tag{4}$$

where p is the dynamic pressure, τ_{ij} is the subgrid stress tensor, ν is the kinematic viscosity and P_x is a uniform pressure gradient in the x-direction that drives the flow. It should be noted that this is not intended as a low-Reynolds-number model; the viscous term is only important in a thin layer near the wall and is included principally to impose the no-slip boundary condition.

The subgrid turbulence model uses a turbulent kinetic energy transport equation based on the second-order closure model of Lewellen (1977). The subgrid velocity variance, q^2, is obtained from the conservation equation

$$\frac{\partial}{\partial t}\left(V q^2\right) + \frac{\partial}{\partial \tilde{x}_i}\left(V G^{ij} u_j q^2\right) = -\tau_{ij} V D_{ij} - \frac{\partial}{\partial \tilde{x}_i}\left(V G^{ij} F_j\right) - \nu \frac{\partial}{\partial \tilde{x}_i}\left(G^{ij}\frac{\partial}{\partial \tilde{x}_k}\left(V G^{kj} q^2\right)\right) - 2bV\frac{q^3}{\Lambda}, \tag{5}$$

where F_i is the subgrid flux, Λ is the subgrid turbulence lengthscale (or filter scale) and the velocity deformation tensor is given by

$$VD_{ij} = \frac{\partial}{\partial \tilde{x}_k}\left(VG^{kj}u_i + VG^{ki}u_j\right). \tag{6}$$

The first term on the right-hand side of (5) represents subgrid turbulence production due to gradients in the resolved velocity field, the next two terms represents transport due to diffusive fluxes and the last term models the dissipation. The subgrid fluxes are given by

$$V\tau_{ij} = S_m q \Lambda V D_{ij}, \tag{7}$$

$$VF_i = S_H q \Lambda \frac{\partial}{\partial \tilde{x}_j}\left(VG^{ji}q^2\right). \tag{8}$$

The various empirical model constants are taken from Lewellen (1977) so that $b = 0.125$, $S_m = \frac{1}{4}$ and $S_H = \frac{1}{3}$.

Finally, the subgrid lengthscale is specified algebraically by

$$\frac{1}{\Lambda^2} = \frac{1}{l^2} + \frac{1}{\Lambda^2_{max}}, \tag{9}$$

where l is a function of distance normal to the nearer of the top or lower bounding surfaces and Λ_{max} is problem dependent. The philosophy of Mason & Callen (1986) is followed in setting the subgrid filter scale independent of the numerical grid, subject to the requirement that the resulting large-scale eddies are adequately resolved. While, in principle, one could use an arbitrarily fine grid for a fixed filter scale, in practice, the idea is to reduce the lengthscale more or less in proportion with the grid size so that smaller-scale turbulent eddies will be resolved. The wall function l is simply set proportional to normal distance in infinite-Reynolds number applications. However, it was found that the lengthscale must be damped more rapidly as the wall is approached when imposing a zero-slip boundary condition for finite-Reynolds number flow. Therefore, following Moin & Kim (1982), we use the Van Driest exponential damping function such that

$$l = \alpha n(1 - \exp(-n^+/A^+)), \tag{10}$$

where n is distance normal to the nearest wall, $\alpha = 0.65$ from Lewellen (1977), $A^+ = 25$, $n^+ = n\tau_0^{1/2}/\nu$ and τ_0 is the local instantaneous wall shear stress.

2.2. *Numerical implementation*

The numerical scheme is similar to that used in the Cartesian model (Sykes & Henn 1989), although the coordinate transformation introduces a number of new terms and other complications; details of the implementation generally follow Clark (1977). The model uses a standard second-order accurate, finite-difference energy-conserving scheme on a staggered grid with leapfrog time differencing. A small amount of smoothing (1%) is used to couple the two time levels and prevent the time-splitting instability. Diffusion terms are modelled using central differencing with the DuFort–Frankel approximation to provide stable integration. The DuFort–Frankel scheme is second-order accurate and consistent with the advection–diffusion equation if $d = K(\Delta t/\Delta z^2)$ is small, where K is the total diffusivity. At the wall, $K = \nu$ and d is less than 0.05 for all cases. In fact, d is generally less than 0.01 over most of the domain since the timestep, which is limited by the vertical Courant condition near the wall, is small. The grid spacing is uniform horizontally but varies vertically, with fine resolution at the walls expanding to a section of uniform spacing comparable to the horizontal spacing.

The elliptic equation for the pressure field is obtained by applying the finite-difference approximation of the divergence operator (3) to the partially advanced velocity fields, i.e. including all terms from (4) except the pressure gradients. The pressure field is then computed from the resulting equation such that zero divergence of the velocity field is maintained. However, the non-orthogonal coordinate transformation makes the equation non-separable, so the direct solver of the Cartesian model must be used in an iterative scheme, as in Clark (1977) and Krettenauer & Schumann (1992). The pressure equation is written in the form

$$L_0(p) = N(p) + D(\tilde{u}_i), \tag{11}$$

where L_0 is the finite-difference representation of the Cartesian Laplace operator (i.e. the case with $h = 0$), N represents the terms of the operator resulting from the coordinate transformation and D is the numerical divergence operator, here applied to the partially advanced velocity fields (denoted by a tilde). The solution is obtained using the direct Cartesian solver for each iteration of the system

$$L_0(p^{(n+1)}) = N(p^{(n)}) + D(\tilde{u}_i), \tag{12}$$

where the superscripts denote iteration and the previous timestep value is used as the initial guess $p^{(0)}$. The iteration continues until the maximum change in p is less than 10^{-5} times the maximum value of p in the domain. The rate of convergence depends on the wave slope since N is generally proportional to the square of the slope. For the maximum slope of 0.628 considered here, convergence requires five to seven iterations.

2.3. *Boundary conditions*

Periodic boundary conditions are imposed at all lateral boundaries. A no-slip condition is imposed on the lower wall by setting u and v below the surface equal and opposite to the values on the first level above the surface. For some of the flows described in the next section, a no-slip condition is also imposed on the upper wall. However, since the flow details at the top of the channel are generally not of primary interest, the upper boundary is usually treated as a rough wall. In this case, a logarithmic profile is used to relate the top wall shear stress to the tangential velocity half a grid length below the wall.

The momentum fluxes at the lower surface are determined by the no-slip condition at the wall and by assuming flow parallel to the wall at the first grid level. The total momentum flux is given by

$$\tau_0 = \nu |u_i^s| z_n^{-1}, \tag{13}$$

where $u_i^s = (u_s, v_s, h_x u_s + h_y v_s)$ is the velocity vector located half a grid length above the lower surface, h_x and h_y are the surface slopes in the x- and y-directions, respectively, and z_n is the normal distance to the wall. Note that for the purpose of setting the wall stress, w is defined in (13) so that u_i^s is parallel to the lower surface. The normal distance is related to the transformed vertical grid spacing at the wall, $\Delta\tilde{z}_0$, by,

$$z_n = \frac{J\Delta\tilde{z}_0}{2(1 + h_x^2 + h_y^2)^{1/2}}. \tag{14}$$

In a local coordinate system defined by the unit surface normal $\hat{n}_i$ and the unit vector in the direction of the tangential velocity, $\hat{u}_i = u_i^s |u_i^s|^{-1}$, the full stress tensor at the surface is

$$\boldsymbol{\tau}_s' = \tau_0 \begin{bmatrix} 0 & 0 & 1 \\ 0 & 0 & 0 \\ 1 & 0 & 0 \end{bmatrix}, \qquad (15)$$

where the prime denotes the local coordinate system. The stress tensor (15) must be rotated into the global Cartesian frame since the momentum equations use the Cartesian velocity components. Using the fact that $h_y = 0$, this rotation results in

$$\boldsymbol{\tau}_s = \frac{\nu}{J\Delta\tilde{z}_0/2} \begin{bmatrix} -2h_x u_s & -h_x v_s & (1-h_x^2)u_s \\ -h_x v_s & 0 & v_s \\ (1-h_x^2)u_s & v_s & 2h_x u_s \end{bmatrix} \qquad (16)$$

which defines the lower boundary condition for the total stress tensor, $\tau_{ij} + \nu D_{ij}$.

The pressure boundary condition is set to ensure consistency between the numerical discretizations of the momentum equation (4) and the pressure source term N from (11) when imposing the constraint of zero normal flow at the wall. By requiring that both u_i and $\tilde{u}_i$ (the partially advanced velocity used in (11)) satisfy this constraint, we obtain a numerical expression of the form $\delta_z p + f(\overline{p}^z) = 0$ for $\tilde{z} = 0$, where δ_z denotes a vertical finite difference and f is a function of the vertically averaged pressure $\overline{p}^z$. The numerical expression for the pressure source term is given by $N = \delta_z f + N_H(\delta_z \overline{p}^z)$, where N_H is a horizontal difference operator. Thus, setting $\delta_z p = 0$ and $f = 0$ at $\tilde{z} = 0$ provides all the necessary boundary conditions for the pressure solver while maintaining consistency with the zero normal flow condition.

3. Flow parameters

The principal focus of this investigation is the configuration of BHA, i.e. channel flow over an infinite array of two-dimensional large-amplitude sinusoidal waves. However, since this LES model had not previously been applied to flows at finite-Reynolds numbers, a flat channel with $Re \approx 12\,000$ was first simulated to test model performance. Then, to test the model with the transformed equations, channel flow over a small-amplitude wavy surface was calculated. Additionally, intermediate wave amplitude configurations were examined as part of a limited investigation into variations of surface pressure, drag, turbulence intensity and flow separation with wave slope.

3.1. *Numerical experiments*

The basic flow geometry is illustrated in figure 1 and all configurations are summarized in table 1. For the wavy surface cases, the standard computational domain contains two wavelengths; test calculations with a single wave (not shown) gave quite different results whereas calculations with four waves were very similar to the standard domain results. This can be seen from the values for case BHA1L given in table 3 (form drag) and table 4 (variance perturbations) which agree within 10 % of the standard domain case BHA1. Note also that grid resolutions for the $2a/\lambda = 0$, 0.031 and 0.2 cases are varied along with the subgrid lengthscale to demonstrate numerical convergence.

The vertical resolution requirements are fairly stringent near the wall, requiring that the lowest grid level be in the viscous sublayer below $z^+ \approx 10$ (using local wall scaling). Using the experimental results to estimate the maximum mean wall shear stress, it was determined that grid levels below $\tilde{z}/H \approx 0.005$ and 0.01 were required

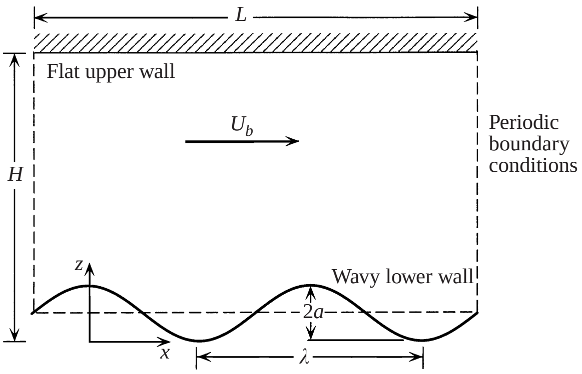

FIGURE 1. Schematic diagram of channel flow over a periodic wavy lower wall. The maximum channel depth is H; the LES computational domain has a length L. For most cases with a wavy surface, L is twice the wavelength λ, the transverse computational width, W, is equal to λ and $\lambda \approx H$. For the flat channel cases, $L = 2H$ and $W = H$.

Case	L	W	λ	$2a/\lambda$	Grid size	$\Delta\tilde{z}_{min}$	$\Delta\tilde{z}_{max}$	Λ_{max}	Re
F	2	1	∞	0	48 × 48 × 90	0.002	0.02	0.005	11 810
FR	2	1	∞	0	80 × 80 × 90	0.002	0.02	0.003	11 820
S1	2	1	1	0.031	48 × 48 × 91	0.002	0.02	0.005	6 560
S1R	2	1	1	0.031	80 × 80 × 102	0.002	0.02	0.003	5 720
S2	1.984	0.992	0.992	0.050	48 × 48 × 71	0.00124	0.0248	0.00620	11 050
S3	2.034	1.017	1.017	0.100	48 × 48 × 71	0.00127	0.0254	0.00636	10 580
S4	2	1	1	0.125	48 × 48 × 67	0.0025	0.025	0.00625	10 800
BHA1	2.143	1.072	1.072	0.200	48 × 48 × 71	0.00134	0.0268	0.00670	10 600
BHA1R	2.143	1.072	1.072	0.200	80 × 80 × 99	0.00134	0.0167	0.00402	10 450
BHA1L	4.286	1.072	1.072	0.200	96 × 48 × 71	0.00134	0.0268	0.00670	12 000
BHA2	2.143	1.072	1.072	0.200	48 × 48 × 71	0.00134	0.0268	0.00670	5 990
BHA3	2.143	1.072	1.072	0.200	48 × 48 × 71	0.00134	0.0268	0.00670	20 060

TABLE 1. Non-dimensional parameters for the various LES calculations, listed in order of increasing slope. L, W, and λ are the streamwise length (x-direction), transverse width (y-direction) and wavelength, respectively; $\Delta\tilde{z}_{min}$ and $\Delta\tilde{z}_{max}$ are the minimum (at the lower wall) and maximum vertical transformed grid sizes, respectively; Λ_{max} is the maximum subgrid filter lengthscale; and the Reynolds number is defined by $Re = U_b\delta/\nu$, where δ is the channel mean half-height and U_b is the bulk velocity, defined in the text. All lengths are normalized by the mean channel depth, $H - a$. The computational grid sizes are given as the number of grid points in the streamwise, transverse and vertical directions, respectively.

for the BHA and flat configurations, respectively. The minimum vertical grid spacings shown in table 1 are less than these estimates to accommodate fluctuations in local wall stresses resulting from very thin viscous shear layers.

All cases were initialized from previous fully turbulent runs and continued until an approximate equilibrium between the imposed constant streamwise pressure gradient and the wall stresses, including pressure forces, was attained. The statistics for all cases presented below are from periods after this equilibrium was reached. Averaging was done over a time of $30H/U_b$ or longer, as well as the lateral coordinate and position of equal phase relative to the surface wave. (The flat cases were averaged over the lateral and streamwise coordinates.) The velocity scale used here is given by

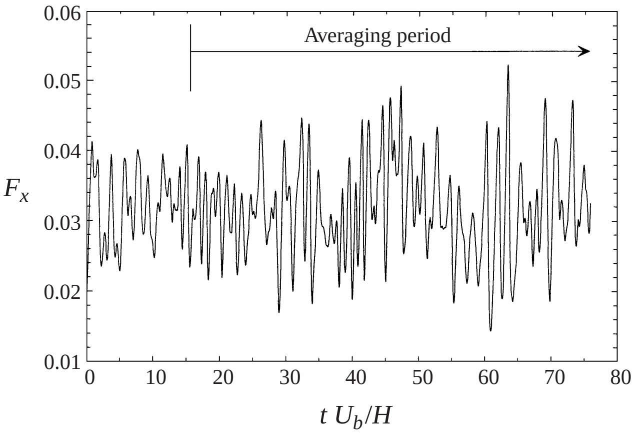

FIGURE 2. Time-history of integrated surface pressure force or form drag, defined by (19) for case BHA1. The averaging period used to generate steady-state statistics is shown on the figure.

a bulk velocity that is independent of streamwise location:

$$U_b = (H - a)^{-1} \int_h^H \bar{u}\,\mathrm{d}z, \tag{17}$$

where the overbar denotes averaging. Henceforth, it will be assumed that all velocities are normalized with respect to U_b.

To check that the flow was sufficiently stationary for computing steady, long-time averages, the time evolution of U_b and the total pressure and shear stress forces at the walls were monitered. As an illustration, figure 2 shows the time history of the integrated surface pressure force, defined in equation (19), for case BHA1. High-frequency (period $\approx H/U_b$) and low-frequency (period $\approx 20H/U_b$) fluctuations are apparent. Nonetheless, it is evident that a meaningful long-time average can be defined over the averaging period shown on the figure.

All simulations were performed on a Windows NT workstation employing a DEC Alpha 21164 300 MHz processor. For the standard BHA1 case (48 × 48 × 71 grid), a single step takes about 7 cpu s. Thus, with a non-dimensional timestep of 8.6×10^{-4}, the integration to a time of 75 took approximately 170 cpu h. By comparison, the flat channel case F(48 × 48 × 90 grid) requires about 5.5 cpu s per step; with a timestep of 3.7×10^{-3} and an integration time of 166, the total run time was about 69 cpu h.

It will be noted that the Reynolds numbers in table 1 do not match the experimental values exactly. Since P_x is held constant throughout the integration, the final bulk velocity and, hence, Reynolds number cannot be controlled directly, but results from the balance between wall stresses and imposed pressure gradient.

In presenting the LES results, the resolved turbulence fluctuations are defined as $\overline{u_i''u_j''}$ where $u_i'' = u_i - \overline{u_i}$ while the total fluctuations include the subgrid components, $\overline{u_i'u_j'} = \overline{u_i''u_j''} - \overline{\tau_{ij}}$. We also define the r.m.s. streamwise velocity fluctuations as $\sigma_u = (\overline{u'^2})^{1/2}$, and similarly for v and w. Note that in presenting results for the flat channel and small-amplitude wave, wall scaling is denoted by a superscript '+', i.e. velocities are normalized by $u_* = \left(\langle\overline{\tau}_0\rangle\right)^{1/2}$ and heights by ν/u_*, where angle brackets indicate averaging over a wavelength.

Reference	Measurements	Re	$2a/\lambda$	Observed features
Frederick & Hanratty (1988)	Mean and fluctuating streamwise velocity (LDV)	6 400	0.031	Linear shear stress response
Hudson *et al.* (1996)	Mean and fluctuating streamwise and vertical velocities, Reynolds stress (LDV)	3 380	0.100	Separated flow
Zilker & Hanratty (1979)	Mean streamwise velocity, wall pressure, wall shear stress (split-film thermal probes, pressure taps, electro-chemical surface probes)	29 300	0.05	Instantaneous reverse flow, nonlinear stress response.
		14 730	0.125	Separated flow
		30 000	0.125	
		30 530	0.200	
Buckles *et al.* (1984, 1986)	Mean and fluctuating streamwise velocity, wall pressure (LDV and pressure taps)	12 300*	0.125	Separated flow
		10 700*	0.200	

TABLE 2. Summary of relevant experiments of flow over wavy surfaces conducted in the laboratory of Hanratty and coworkers. The measurement techniques are given in parentheses.

* These Reynolds numbers have been modified from their published values to conform with the bulk velocity definition (17). See §6 for further discussion.

3.2. *Laboratory experiments*

As mentioned in the introduction, Hanratty and coworkers at the University of Illinois have presented an extensive set of measurements of channel flow over wavy surfaces; those referred to in this paper are summarized in table 2. The experiments cover a wide range of slopes and Reynolds numbers since the nature of the flow depends strongly on these parameters, as illustrated in the flow regime map presented by Kuzan *et al.* (1989). We have concentrated on experiments with $Re \approx 10^4$ where the mean flow separates for $2a/\lambda$ somewhat greater than 0.05.

All experiments were conducted in a rectangular water channel with a cross-section of 5.08×61 cm^2. A long flat section preceded a sinusoidal wavetrain machined into the lower channel wall such that the mean cross-section was unchanged. The flat section was long enough that the flow was fully turbulent before encountering the first wave and the channel wide enough for the mean flow to be essentially two-dimensional. Spatially periodic flow was established fairly rapidly; measurements were typically taken over the eighth wave in a series of 10. (The measurements of Hudson *et al.* (1996) were taken over the 31st of 36 waves.)

4. Flat channel

We first present results for a flat channel at $Re \approx 12\,000$ with no-slip boundary conditions at both walls, similar to the LES study of Moin & Kim (1982). Figure 3 shows the mean streamwise velocity profiles for cases F and FR compared with the data of Hussain & Reynolds (1970). The calculated profiles are in reasonable agreement with the data, with only a slight underprediction evident in the outer part of the wall layer ($z^+ \approx 10$ to 30). The profiles show very little sensitivity to resolution, an indication of numerical convergence. LES profiles from only the lower wall are

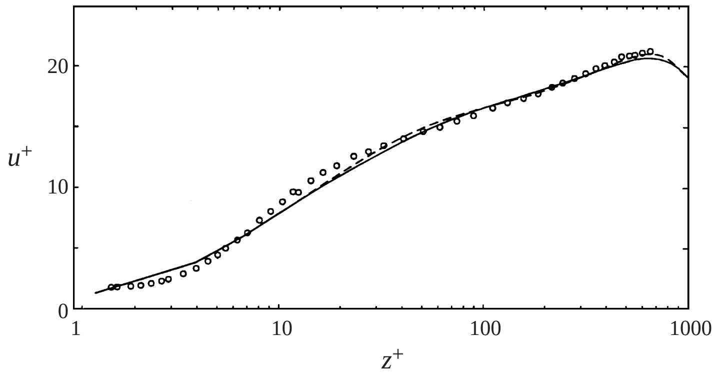

FIGURE 3. Mean velocity profile for flat channel cases compared with experimental data: ——, standard resolution case F; — — —, higher resolution case FR; ○, measurement of Hussain & Reynolds (1970). $Re = 3\,800$.

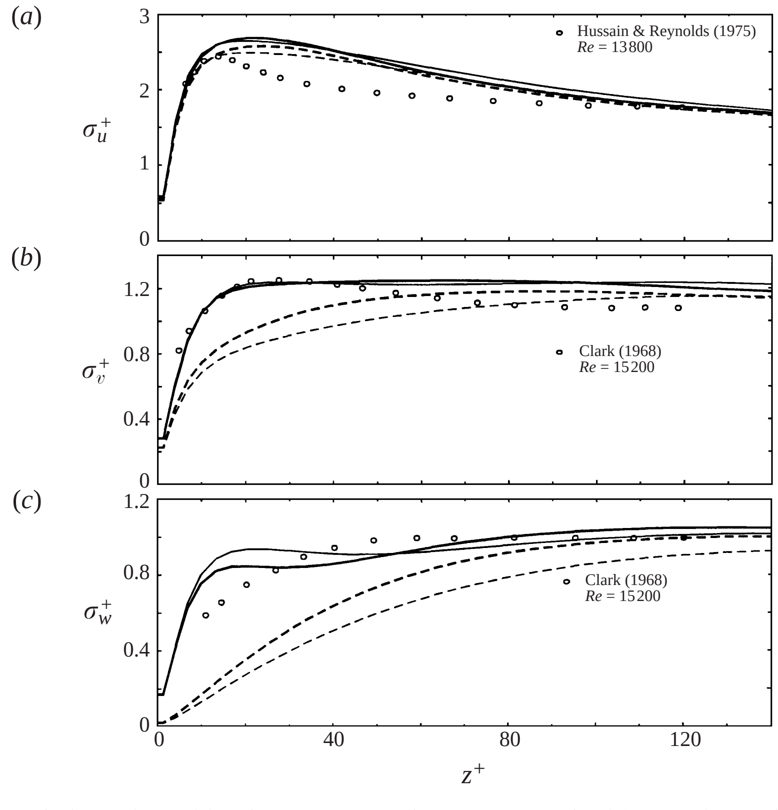

FIGURE 4. Turbulence intensities for cases F and FR compared with experimental data: ——, total fluctuations; — — —, resolved components. The high resolution case FR is shown with bolder lines. (*a*) Streamwise turbulence intensity, (*b*) transverse turbulence intensity, (*c*) vertical turbulence intensity.

plotted, but those from the upper wall are virtually indistinguishable, an indication of adequate statistical averaging.

Figure 4 shows profiles of the turbulence intensities, resolved and total, in the vicinity of the wall whereas figure 5 shows the profiles over the lower half of the

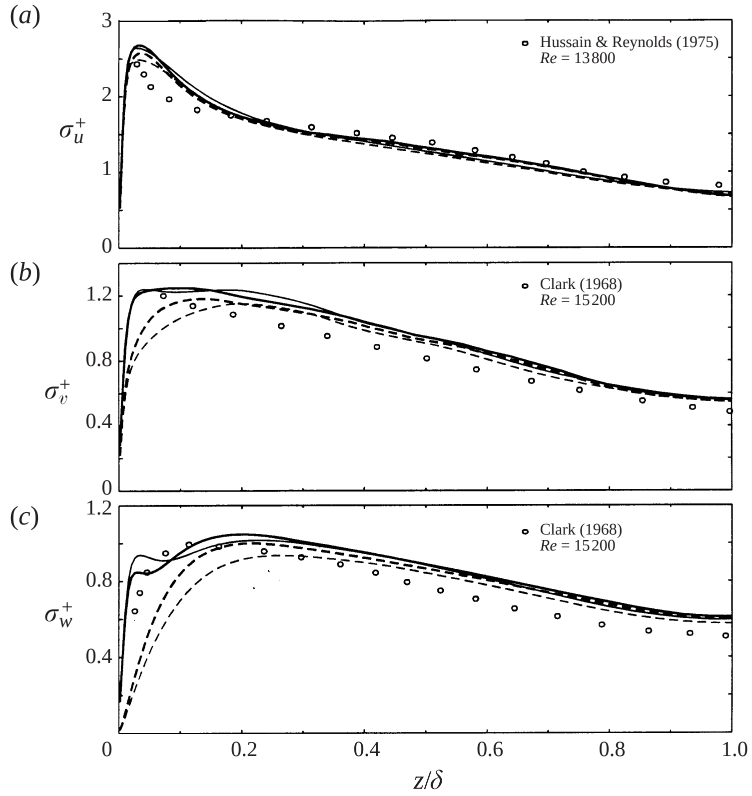

FIGURE 5. As figure 4, but height above wall scaled by channel half-depth. (*a*) Streamwise turbulence intensity, (*b*) transverse turbulence intensity, (*c*) vertical turbulence intensity.

channel. The peak values near the wall match the experiments well, as do the values in the middle of the channel. The streamwise intensity is somewhat overpredicted for $z^+ \approx 20$ to 80, since the LES shows a more gradual fall off from the near-wall peak. It is evident that the vertical intensity prediction is determined principally by the subgrid model near the wall; τ_{33} increases too rapidly from the wall but nonetheless shows good agreement overall. It can be seen that the resolved components increase as the subgrid filter scale is reduced but the total intensities are not significantly changed, indicating an appropriate transfer of energy from the subgrid to the resolved component as resolution is increased. The agreement with the experimental data is comparable to the LES of Moin & Kim (1982).

5. Small-amplitude wavy surface

Before presenting results for the large-amplitude wave, we simulate flow over a small-amplitude wave that tests the coordinate transformation while still yielding results close to the flat channel. This flow is of interest in its own right, so we will compare with experimental and theoretical results. This will enable us to examine the model predictions without the complicating effects of separation.

5.1. *Mean velocity*

Results from cases S1 and S1R, with $2a/\lambda = 0.031$, are compared with the measurements of Frederick & Hanratty (1988). Figure 6 shows the wavelength-averaged mean

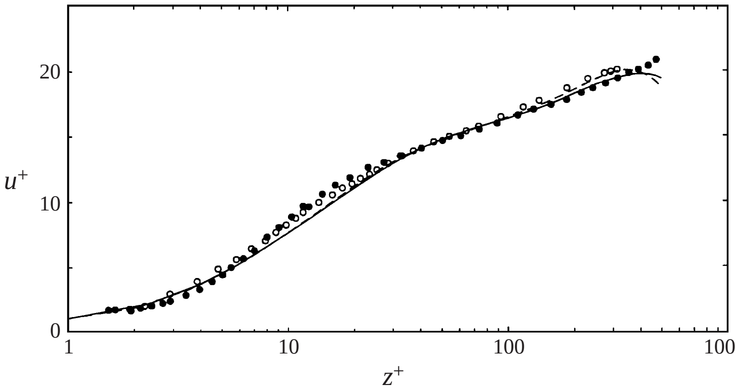

FIGURE 6. Mean wavelength-averaged velocity profile for cases S1 and S1R ($2a/\lambda = 0.031$) compared with experimental data. ——, standard resolution case S1; — — —, higher-resolution case S1R; ○, Frederick & Hanratty (1988), $Re = 6400$; ●, Hussain & Reynolds (1970), $Re = 13\,800$.

streamwise velocity. The LES results are averaged along lines of constant η while the data are averaged along lines of constant height above the wave surface. For this small slope, the difference between the two averaging definitions is negligible. The predicted profiles are generally in close agreement with the measurements and the two numerical resolutions result in nearly identical profiles. As with the comparison shown in figure 3 for the flat channel, the LES profiles are somewhat low over the approximate range $10 < z^+ < 30$, although the discrepancy is slightly less here. The flat channel data of Hussain & Reynolds (1970) are also shown in the figure; it is evident that the wavelength average matches these data quite closely, as would be expected for linear perturbation at this small slope.

The velocity profiles at different locations along the wave are shown in figure 7. Profiles are paired such that they should be symmetric around the wavelength average (shown as a dashed line), assuming perfectly linear behaviour. The overall agreement with the data is good, particularly above the viscous sublayer, $z^+ > 10$. The largest discrepancies occur near the surface of the upslope profiles at $x/\lambda = 0.6$ and 0.7, where the measurements show greater flow acceleration. It seems that the LES predictions in these cases show more linear behaviour, i.e. the paired LES profiles are more nearly symmetric about the wavelength average than the experimental data.

In a study of flow over hills using second-order closure and mixing-length models, Newley (1985) examines the streamwise velocity perturbation profile above the wave crest and finds that the maximum can be expressed as

$$\Delta u_{max} = \frac{\beta u_0^2(l_0)}{aku_0^2(l_m)}, \tag{18}$$

where u_0 is the unperturbed mean streamwise velocity, ak is the maximum slope, wavenumber $k = 2\pi/\lambda$, l_m is the height of the maximum perturbation above the crest, l_0 is an outer layer scale set to k^{-1} for periodic hills and β is an $O(1)$ constant. A fit to the second-order closure results gives $\beta \approx 1$ (and $\beta \approx 0.8$ for the mixing-length model). The LES results, using the wavelength average velocity for u_0, give $\beta = 1.5$. This discrepancy partly reflects the fact that l_m is higher with the LES model: $l_m/\lambda = 0.013$ compared with approximately 0.006 for Newley's second-order closure calculations for hills with similar slopes. Of course, Newley's calculations are for rough surfaces, so these results are not directly comparable, especially since l_m is just

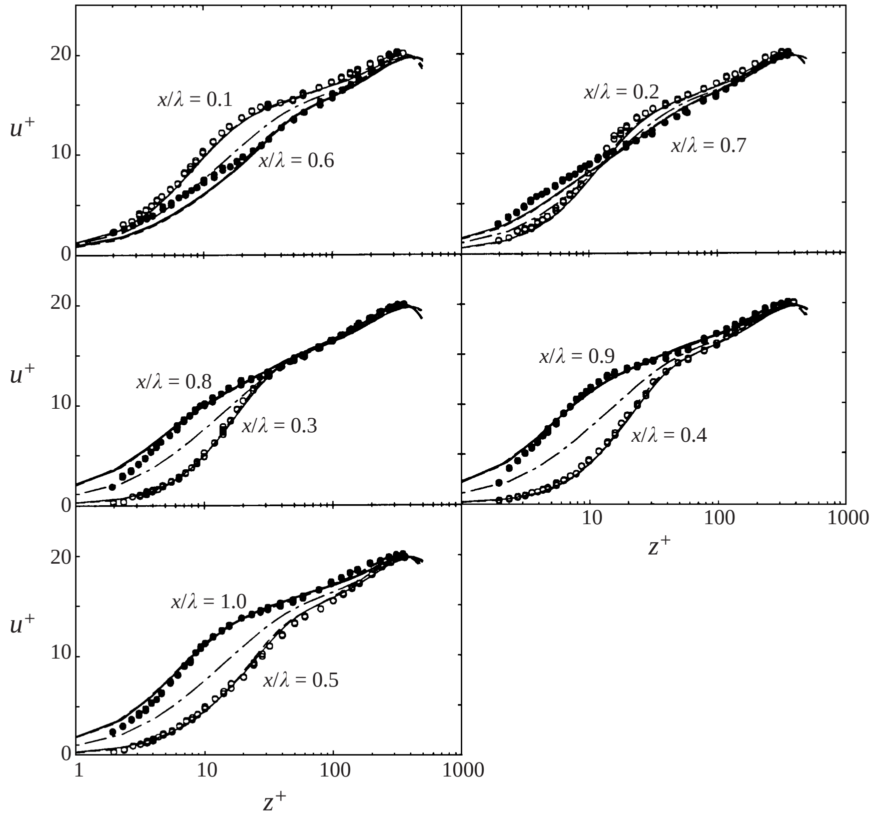

FIGURE 7. Profiles of mean streamwise velocity at various locations along the surface wave compared with data of Frederick & Hanratty (1988). For the downslope locations $x/\lambda = 0.1$ to 0.5, thin solid lines are case S1, thin dashed lines are case S1R and open circles are the experimental data. For the upslope locations $x/\lambda = 0.6$ to 1.0, thick solid lines are case S1, thick dashed lines are case S1R and solid circles are the experimental data. The wavelength average from S1R is shown with the long-dash, short-dash pattern. (The curves from the two LES cases are virtually indistinguishable.)

barely above the viscous sublayer. If we re-examine the data of figure 7 in terms of the perturbation velocity near the surface, as is done in Frederick (1986), we see that the prediction of l_m matches the experiment quite well. As can be seen from figure 8, the LES profiles at the wave crest and trough show good overall agreement with the data, although the overprediction at $x/\lambda = 0.5$, $z^+ > 10$ is more noticeable with the linear scale. The maximum perturbations above the crest are only about 10 % higher than the experimental values, indicating that the LES prediction of β is reasonably consistent with the experimental data.

5.2. *Turbulence intensity*

Streamwise turbulence intensity measurements from Frederick (1986) are shown in figure 9 along with the LES results. The predictions compare favourably overall with the experiment in that the basic variations with location are reproduced. The turbulence intensities generally are out of phase with the pressure gradients: a positive (adverse) pressure gradient has a destabilizing effect and hence increases the velocity fluctuations whereas the opposite is true for negative (favourable) pressure gradients. Thus, the peak values increase from profiles at $x/\lambda = 0.1$ to 0.5 and decrease

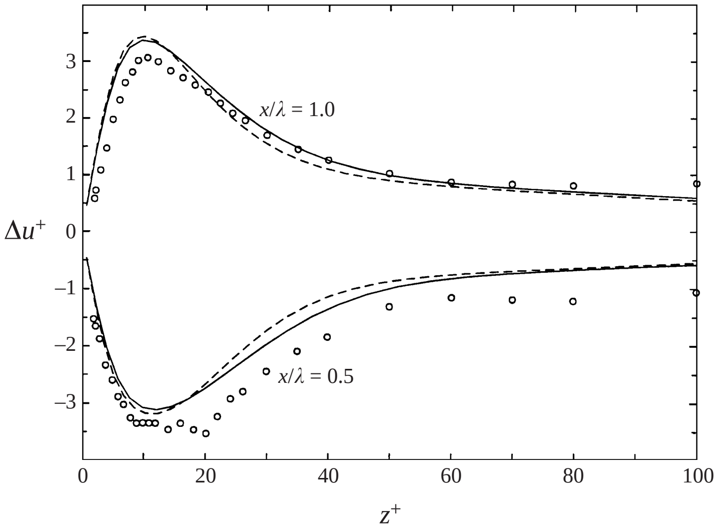

FIGURE 8. Profiles of mean streamwise velocity perturbation at the wave crest and trough. ——, case S1; — — —, case S1R; ○, experimental data of Frederick (1986).

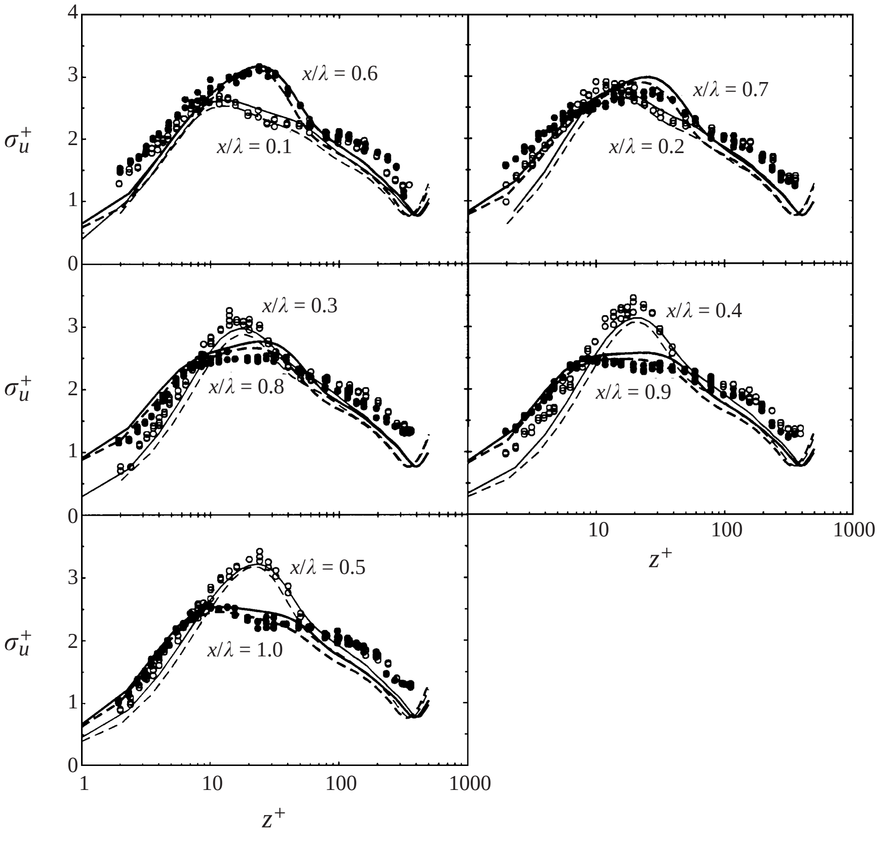

FIGURE 9. Profiles of mean streamwise turbulence intensities from cases S1 and S1R at various locations along the surface wave compared with the data of Frederick (1986). Line patterns and symbols as in figure 7 (but the wavelength average is not shown here).

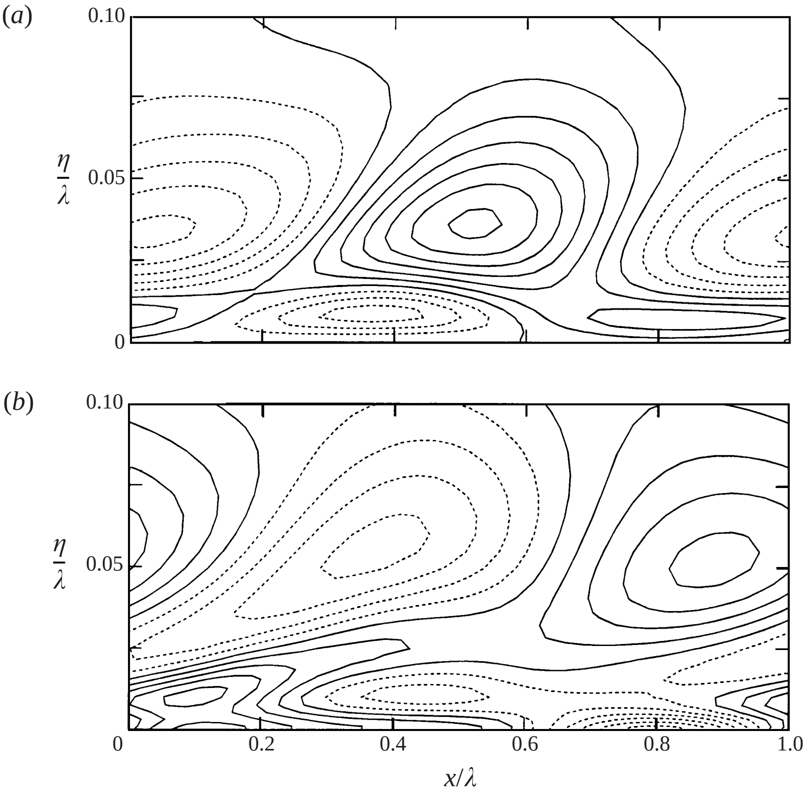

FIGURE 10. Velocity variance perturbation from the wavelength average, normalized by u_*^2, for case S1R. (*a*) Streamwise component; contour interval is 0.4. (*b*) Vertical component; contour interval is 0.04. Dashed lines indicate negative values.

thereafter to $x/\lambda = 1$. The LES peak values match the measurements quite well regarding both magnitude and location (typically around $z^+ \approx 20$). Near the wall, the LES predictions are generally low and show greater differences between the paired profiles. Away from the wall, $z^+ > 100$, the LES also tends to underpredict the fluctuation intensity. However, flat channel measurements from the same facility (Frederick 1986) show 10–20 % greater centreline intensities than typically given in the literature, e.g. Hussain & Reynolds (1975).

To relate the LES results to some of the theoretical models of flow over small-amplitude waves (e.g. Sykes 1980; Newley 1986), we show the streamwise and vertical velocity variance perturbation fields for the high-resolution case S1R in figure 10. (The transverse component will be discussed in §9.) The streamwise component is defined as $\Delta\overline{u'^2} = \overline{u'^2} - \langle\overline{u'^2}\rangle$, with the vertical component defined similarly. There is qualitative agreement with the closure model predictions: a distinct surface layer is evident; the perturbations maximise above and are almost 180° out of phase with the surface layer; the maximum positive streamwise perturbation occurs over the trough while the largest negative perturbation occurs over the crest. A quantitative comparison with the models is not meaningful owing to differences in the bottom boundary conditions; the inner layers defined in Sykes (1980) and Belcher *et al.* (1993) would both fall within the viscous sublayer of the LES, thus invalidating their assumption of a log profile. It is interesting to note that $\Delta\overline{u'^2}$ above the surface layer

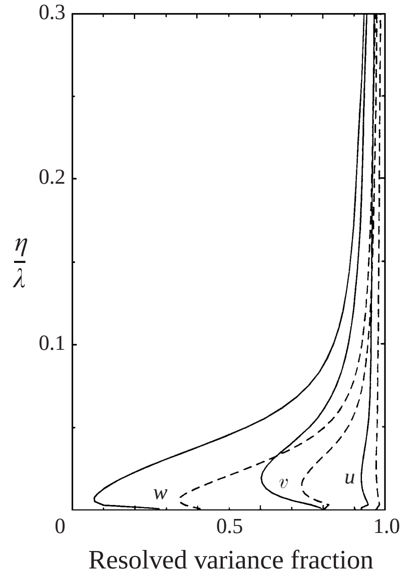

FIGURE 11. Fractions of velocity variances resolved by the LES: ——, standard resolution case S1; — — —, higher-resolution case S1R. The lines labelled u are fractions for the streamwise component (defined in the text); v and w denote the transverse and vertical components, respectively.

is out of phase with $\Delta\overline{w'^2}$. Whereas the streamwise variance decreases over the wave crest, the vertical variance increases there, a result not predicted by closure models or rapid distortion theory but observed in measurements over hills (Belcher *et al.* 1993). It should also be noted that the maximum in $\Delta\overline{u'^2}$ is localized close to the surface compared with $\Delta\overline{w'^2}$. Thus, although the maximum magnitude of $\Delta\overline{u'^2}$ is nearly ten times greater than $\Delta\overline{w'^2}$, it decays rapidly with height and so for the region $\eta/\lambda > 0.1$, the perturbations are of comparable magnitude.

The results shown in figure 10 are determined to some extent by the subgrid model, especially near the surface. Therefore, it is important to examine how much of the total variances are explicitly resolved in the LES. The wavelength-averaged fractions of resolved variances, defined as $\langle\overline{u''^2}\rangle/\langle\overline{u'^2}\rangle$ for the streamwise variance and similarly for the transverse and vertical variances, are shown in figure 11 for cases S1 and S1R. It can be seen that more than 90 % of the streamwise variance is explicitly resolved over the entire domain for both numerical resolutions. In contrast, only 10 % of the vertical variance is resolved very close to the surface in S1 while the minimum resolved fraction of the transverse variance approaches 60 %. Higher resolution results in a noticeable improvement: the minimum resolved fraction increases to 35% for the vertical variance and 75% for the transverse component. In the standard resolution case S1, all components are more than 80% resolved for $\eta/\lambda > 0.1$. This level of resolution is achieved for $\eta/\lambda > 0.05$ with the higher-resolution of S1R. Thus, the variance perturbations shown in figure 10 are essentially resolved above the surface layer; the calculations within the surface layer must be viewed with some caution, however.

5.3. *Surface shear stress*

Zilker (1976) presents surface wall stress data for this flow; a comparison with the LES results is shown in figure 12. The model predictions are close to the measurements

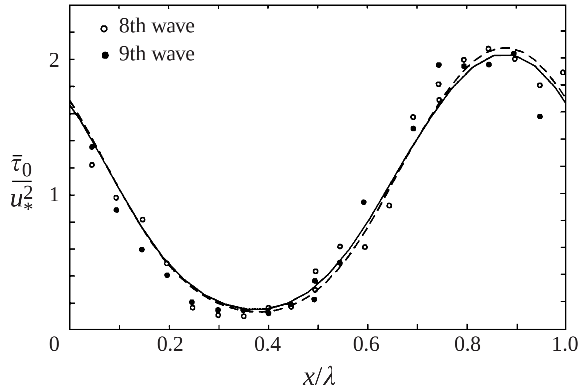

FIGURE 12. Non-dimensional shear stress distributions: ——, case S1; – – –, case S1R; symbols are the data of Zilker (1976) from two adjacent waves.

in both phase and magnitude, although the experimental scatter suggests caution in making any definitive conclusions. It is evident that the wall stress data show a phase lead relative to the wave crest. Fitting the data with a two-harmonic Fourier series, Frederick (1986) finds a phase of 51° for the dominant first harmonic. The LES shows a slightly smaller phase shift of approximately 45°. These results are consistent with theoretical models (e.g. Sykes 1980; Hunt *et al.* 1988), and reflect the fact that the maximum perturbation velocity near the surface is shifted upstream (Newley 1985). The shear stress perturbation is not exactly symmetric: the increase just ahead of the wave crest is of larger magnitude than the decrease that occurs just upwind of the trough. Accordingly, the low-stress region around the trough is of somewhat greater extent than the high-stress region.

6. Separated flow over a large-amplitude wavy surface

We now turn to the BHA configuration, $2a/\lambda = 0.2$, that exhibited a large separated region extending over most of the wave trough. There is some uncertainty in the definition of the bulk velocity used in BHA. They give a definition that is a function of position, which seems to be an unnecessary complication. On the other hand, Buckles (1983) uses a bulk velocity with a normalizing depth equal to the minimum channel depth, $H - 2a$, rather than the mean channel depth. That is also consistent with integrals of the tabulated velocity profiles given in Buckles (1983) and used here for comparison with the LES. Therefore, for this section only, we use a definition of bulk velocity given by

$$U_b = (H - 2a)^{-1} \int_h^H \bar{u}\, \mathrm{d}z.$$

Note that using this definition gives a Reynolds number 12% higher than that obtained with the bulk velocity definition (17). This discrepancy is reflected in the Reynolds numbers given in tables 2 and 3.

6.1. *Mean velocity and streamlines*

Profiles of the mean streamwise velocity for the simulations BHA1 and BHA1R are compared with the experimental data in figure 13. Clearly, both the measurements and the LES show strongly separated flow. The predicted magnitude of the reversed

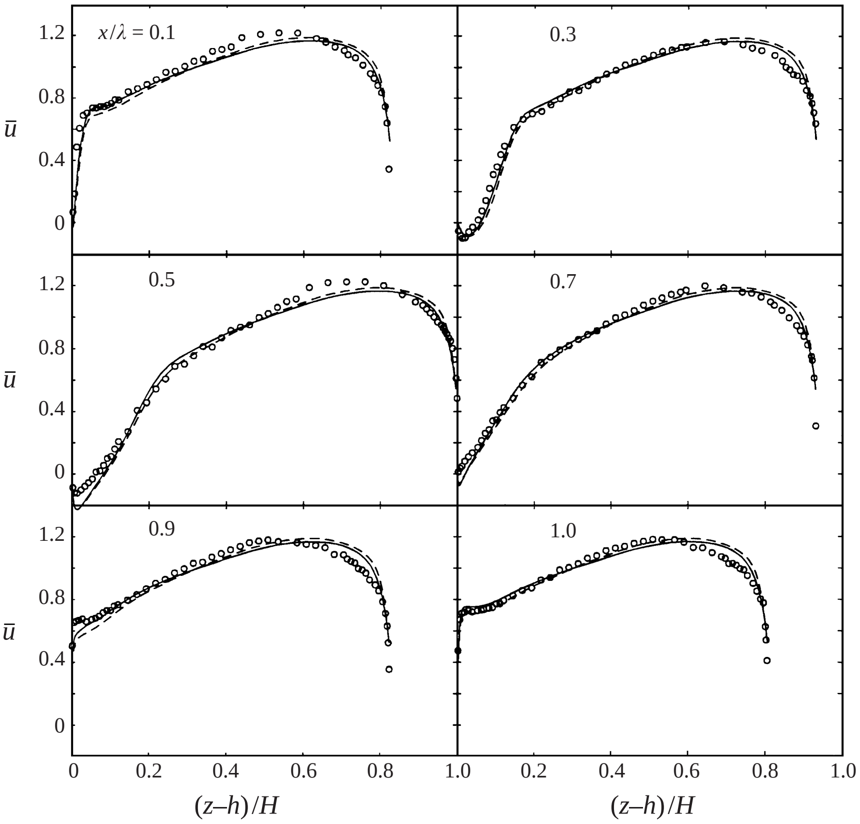

Figure 13. Profiles of mean streamwise velocity at various locations along the surface wave compared with the data of BHA. ——, LES case BHA1; — — —, case BHA1R; symbols are measurements.

flow in the recirculation zone, roughly between $x/\lambda = 0.1$ and 0.7, tends to be slightly greater than observed, but overall the profile variations along the wave are faithfully reproduced. Some locations show an underprediction in the middle of the channel, but this appears to be due to variations in the measurements. We note that the profiles reported by BHA contain discrepancies of up to 3% in the integrated mass flux, which is necessarily conserved in the LES.

Profiles at the crest, trough and two intermediate positions are shown on a log scale in figure 14 to emphasize the near-surface region. The LES profiles (only BHA1R is shown since BHA1 is very similar) are in reasonable agreement with the measured data. In particular, they match well over the crest except for a slight underprediction very close to the surface. Significant shear can be seen very close to the surface at the crest. Above this, the velocity profile is nearly constant for a short while before increasing to the channel centreline maximum. The LES overpredicts the reverse flow in the trough, but shows better agreement on the up- and downslope locations. Note that the LES profiles show slightly negative velocity at $x/\lambda = 0.7$ while the measurements are slightly positive, indicative of a somewhat further downstream reattachment point in the LES.

The mean streamwise velocity field and streamlines are shown in figure 15 for BHA1R. (The results for BHA1 are similar.) The strong shear over the crests is clearly shown, but it should also be noted that there is still significant shear centred

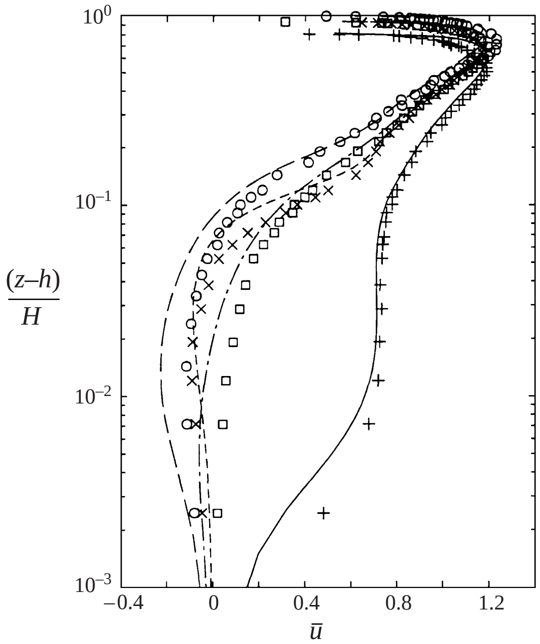

FIGURE 14. Profiles of mean streamwise velocity using a logarithmic vertical axis. Only profiles from BHA1R are shown for comparison with the data. (The profiles from BHA1 are very similar.) The lines denote LES profiles, symbols denote BHA measurements. $x/\lambda = 0.3$: short dashes, ×. $x/\lambda = 0.5$: long dashes, ○. $x/\lambda = 0.7$: long-dash, short-dash, □. x/λ=1: solid line; +.

more or less around the $\Psi = 0$ streamline. The recirculation zone, bounded by the $\Psi = 0$ streamline and the wave surface, is somewhat deeper than that shown in BHA (their figure 5); the bounding streamline has a maximum elevation approximately 90% of the wave height compared with 60% in BHA. Although the LES velocity profiles agree well with the observations over the bulk of the recirculation zone, the overprediction of the reverse flow near the surface results in the integral defining the streamlines, namely,

$$\Psi = \int_h^z \bar{u} \mathrm{d}z',$$

going to zero at a greater height.

A detailed examination of the LES and experimental data shows some discrepancy in the precise extent of the recirculation region. Separation (in the mean flow) occurs at $x/\lambda = 0.14$ in the experiment compared with 0.06 for both BHA1 and BHA1R; reattachment occurs at 0.69 in the experiment and at 0.73 and 0.75 for BHA1 and BHA1R, respectively. Since the experimenters note that velocity measurements are inaccurate very close to the surface (below $z/\lambda \approx 2.6 \times 10^{-3}$), there is some uncertainty in the precise locations of the mean separation and reattachment points. Nonetheless, this discrepancy has little adverse effect on predicting the salient features of the mean flow.

6.2. *Intermittency and flow variability*

It is suggested in BHA that the location of the zero mean streamwise velocity contour corresponds closely with the locus of 50% instantaneous reverse flow, i.e. $\gamma = 0.5$

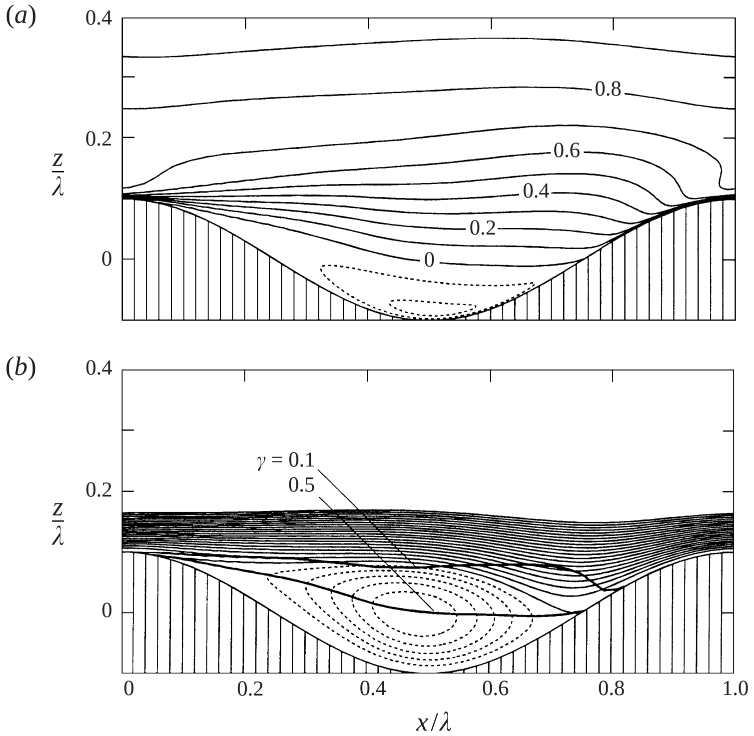

FIGURE 15. Mean flow field statistics from case BHA1R. (*a*) Streamwise velocity, (*b*) streamlines. Negative velocities and streamlines are shown as dashed lines. Also shown in (*b*) are the loci of 10% and 50% instantaneous reverse flow.

where the intermittency γ is defined as the fraction of time that u is positive. This is clearly confirmed for the LES in figure 15, where the $\gamma = 0.5$ line originates very close to the separation point and terminates very close to the point of reattachment, as in BHA. The $\gamma = 0.1$ contour indicates that there is a significant fraction of reverse flow at the top of the mean recirculation zone, i.e. at approximately the height of the wave crests. The location of this line matches well that shown in BHA, although they note that it falls surprisingly high above the recirculation zone. This is not the case with the LES owing to its deeper recirculation zone.

The intermittency contours imply large variability in the flow associated with the recirculation zone. Plots of instantaneous velocity fields, examples of which are shown in figure 16, indicate that large-scale flow features are responsible for this variability. Clearly, flow separation results in large-scale ‘flapping’ of the shear layer as well as other complex behaviour. For example, the character of the flow is strikingly different in each of the four troughs shown in figure 16. In one case, reverse flow fills most of the ‘valley’ above the trough whereas, in another, reverse flow is confined to a shallow region near the wave surface. In a third case, reverse flow seems to have been ejected away from the surface. Finally, we see a number of small areas, typically on the downslope, where the reverse flow appears to have separated so that there is forward flow very near the surface. It is clear from these examples that the mean streamlines are not at all representative of the instantaneous flow, but they do illustrate the region where recirculating flow is likely to be observed.

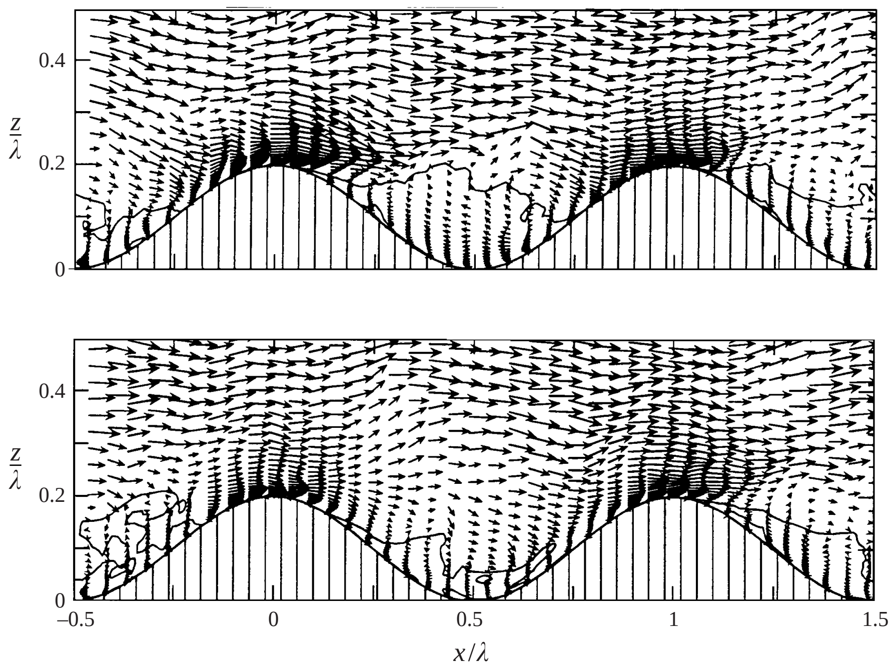

FIGURE 16. Two independent realizations of instantaneous velocity vectors (u, w) at $y = 0$ for case BHA1R. Solid lines denote loci of $u = 0$. Every other grid point is shown. The maximum velocity is approximately 1.4.

6.3. *Higher-order statistics*

The relative streamwise turbulent fluctuations are shown in figure 17, where it can be seen that the LES results are in close agreement with the data. Only the total fluctuation intensities are plotted since the subgrid components are almost negligible everywhere. BHA1R profiles are in close agreement with those of the lower resolution BHA1; there are slight differences in some details, but statistics for the two resolutions differ by less than a few per cent.

The highest fluctuation intensities are associated with the free shear layer that detaches from the surface at the separation point and is elevated above the separation zone. The magnitude of this maximum intensity remains fairly constant over much of the wave. A reduction is seen after the flow reattaches and speeds up as it approaches the wave crest. These features can be seen more clearly in figure 18, where turbulence intensity fields are shown for the three coordinate directions. The locus of maximum streamwise intensity extends over most of the trough at a height equal roughly to the maximum wave height, before elevating somewhat towards the crest. This locus approximately coincides with the midpoint of the vertical shear region in the mean velocity field (see figure 15*a*). The vertical extent of this free shear layer is evident from the ‘elbows’ in the mean velocity profiles of figure 13, particularly for $x/\lambda = 0.3$ and 0.5. The magnitude of the maximum streamwise intensity increases rapidly from a value of about 0.20 very close to the crest to around 0.25 a quarter of the wavelength downstream.

As discussed in BHA, remnants of the free shear layer separating from the upstream wave are manifested as an elevated ($z/H \approx 0.25$ to 0.35) region of increased streamwise turbulence intensity over the wave crest. It can be viewed simply as a continuation

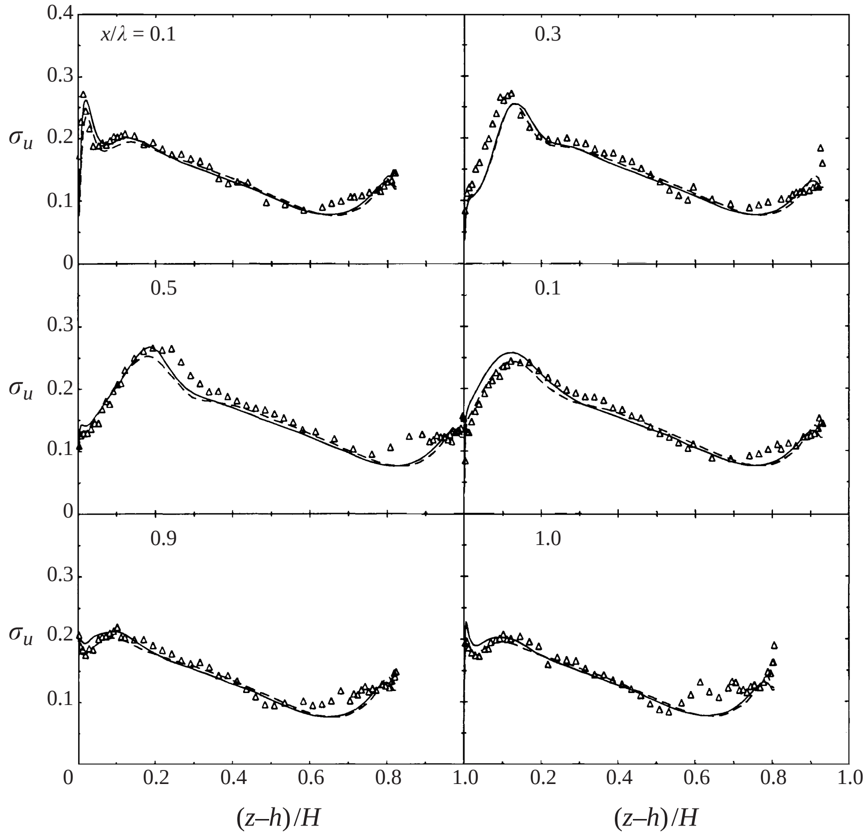

FIGURE 17. Profiles of mean streamwise turbulence intensity at various locations along the surface wave compared with the data of BHA. ——, BHA1; — — —, BHA1R; symbols are measurements. Total LES turbulence intensities are shown.

of the locus of maximum intensity mentioned above through a periodic domain. However, this elevated maximum decays rapidly downstream of the crest.

A moderate increase in the vertical fluctuation intensity, σ_w, above the wave crest may also be associated with the shear layer remnant. However, the maximum intensity occurs over the trough and is probably related to the large-scale eddies responsible for the variations of the separated flow, as illustrated in figure 16.

Unlike σ_u and σ_w, the transverse fluctuation intensity, σ_v, does not show any particular feature associated with the free shear layer. However, there is a very pronounced maximum near the surface on the wave upslope whose effects extend over the downstream crest. This is a feature which seems characteristic of all wavy-surface cases that we have examined. Since it is rather unexpected and, to our knowledge, has not been observed experimentally, we will discuss it further in § 9.

The contour plots of streamwise and vertical turbulence intensities in figure 18 appear qualitatively similar to those shown in Hudson *et al.* (1996) for separated flow over a smaller wave ($2a/\lambda = 0.1$) at a lower Reynolds number ($Re = 3380$). In fact, the locations and even the magnitudes of the maximum observed intensities are reasonably close to the LES predictions. Hudson *et al.* correlate the different locations of σ_u and σ_w maxima with the different direct production terms (involving the Reynolds stresses and mean velocity gradients). They also point out that the lag in vertical intensity

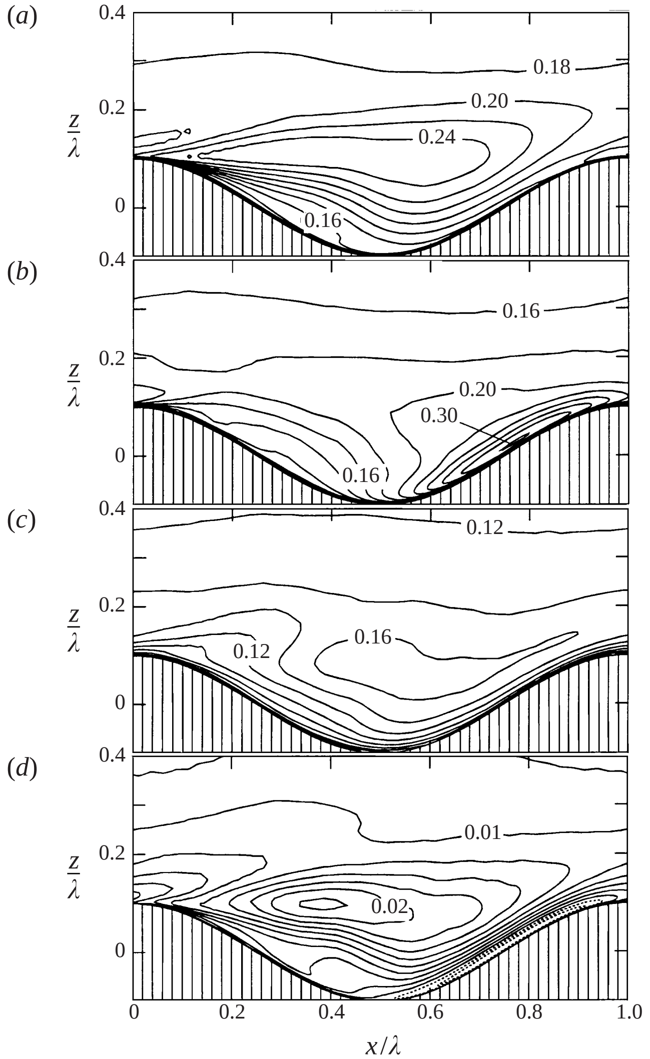

FIGURE 18. Dimensionless mean flow statistics from case BHA1R. (*a*) Streamwise turbulence intensity, σ_u, (*b*) transverse turbulence intensity, σ_v, (*c*) vertical turbulence intensity, σ_w, (*d*) Reynolds stress $-\overline{u'w'}$.

maximum relative to the streamwise intensity is consistent with the initial direct production of streamwise fluctuation (through $\overline{u'w'}\,\partial\overline{u}/\partial z$ and $\overline{u'^2}\,\partial\overline{u}/\partial x$) and the subsequent transfer of energy into vertical fluctuations via the pressure-strain term.

Hudson *et al.* also show contours of the Reynolds stress $-\overline{u'w'}$, which again is in qualitative agreement with the LES results shown in figure 18. It can be seen that the elevation of the maximum Reynolds stress is very close to that of maximum σ_u and is clearly associated with the separated shear layer. The negative values close to the surface on the upslope are an artifact of the Cartesian coordinate system (Hudson 1993); they assume positive values if rotated into a boundary-layer or streamline coordinate system.

Profiles of skewness and flatness of the streamwise velocity, defined as $S = \overline{u''^3}/\sigma_u^3$ and $F = \overline{u''^4}/\sigma_u^4$, respectively, are compared with the BHA data for $x/\lambda = 0.3$

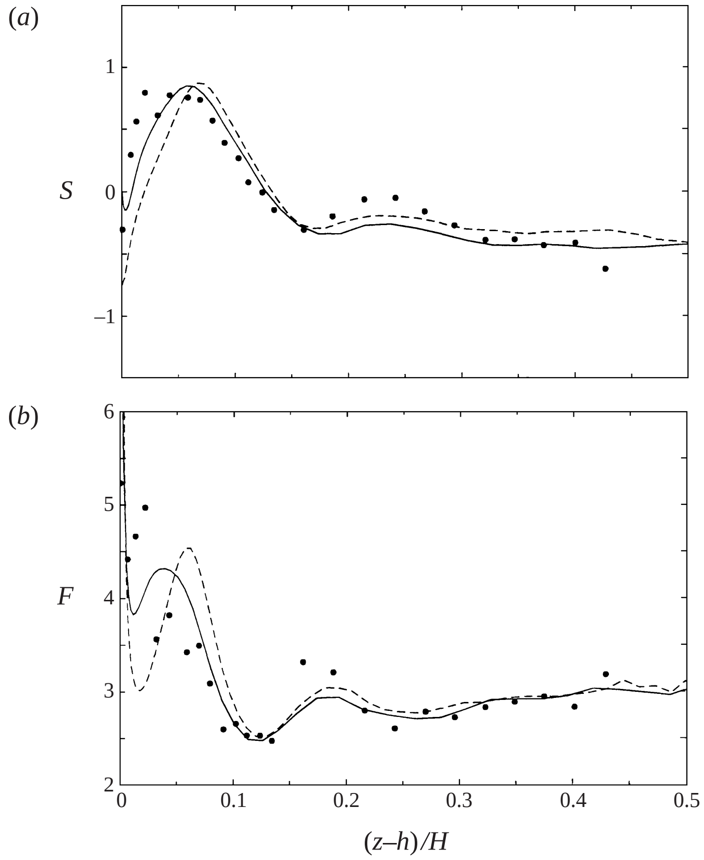

FIGURE 19. Higher-order statistics at $x/\lambda = 0.3$. ——, BHA1; — — —, BHA1R; symbols are data of BHA. (*a*) Skewness. (*b*) Flatness.

in figure 19. The agreement between the LES profiles and the measurements is encouraging considering the difficulty in obtaining reliable higher-order statistics. Away from the wall, the profiles do not differ greatly from those computed or measured previously over a flat wall, e.g. Moin & Kim (1982). The midchannel values of $S \approx -0.4$ and $F \approx 3$ are close to the flat channel values and result from velocity fluctuations produced by slow-moving fluid arriving from the wall region. However, the profiles clearly differ from flat channel flow near the wall. For instance, S decreases from its maximum, which is associated with the elevated shear layer, to a small negative value at the wall. In contrast, the flat channel profile of skewness maximizes at the wall. This is also true for flatness. However, for the BHA flow, F shows some rather complex behaviour close to the wall, particularly around $(z - h)/H \approx 0.05$. While not inconsistent with the measurements, it remains to be seen if this is real or an artifact of the LES model. The LES profiles do show some sensitivity to resolution, especially for F near the wall. This is not surprising since only the resolved velocity fluctuations are considered.

Contour plots of skewness and flatness are shown in figure 20. It can be seen that a region of high skewness occurs just downstream of the crest, reaching its maximum around the separation point. The locus of the maximum skewness seems to follow approximately along the middle of the recirculation zone. Large negative values of

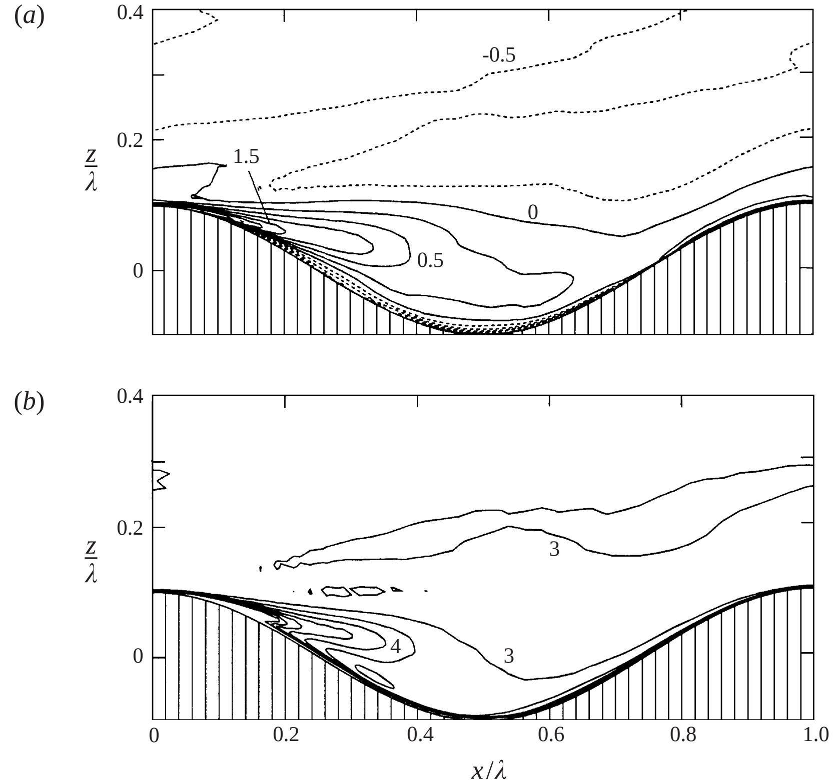

FIGURE 20. (*a*) Skewness; contour interval of 0.25. (*b*) Flatness; contour interval of 0.5.

skewness are seen very close to the wave surface over the region of reverse flow while near-surface positive skewness seems to be associated with attached, forward-moving fluid. Both observations are consistent with the view that velocity fluctuations near the wall are caused by fast-moving fluid being mixed down from above. But, the skewness is then necessarily negative in the reverse flow region. The region of high flatness is closely correlated with the region of high skewness, suggesting that the process of mixing faster-moving fluid to the wall is intermittent.

6.4. *Surface pressure and shear stress*

The final comparisons with BHA are of the pressure and shear stress on the wavy surface. An accurate prediction of these quantities is clearly an important aspect of LES since they determine the integrated forces on the wave, which is of interest in aeronautics, oceanography, meteorology and other fields. Variations of the pressure force with slope are discussed in §8; here we focus on the BHA configuration.

Figure 21 shows distributions of non-dimensional wall pressure p_w and shear stress τ_w compared with the experimentally measured distributions, where

$$p_w = \left(\tfrac{1}{2}U_b^2\right)^{-1}\overline{p}|_{\eta=0}, \quad \tau_w = \left(\tfrac{1}{2}U_b^2\right)^{-1}\overline{\tau}_0.$$

The pressure plots have been adjusted so that the LES and observations match at the wave trough. It can be seen that both BHA1 and BHA1R predict the pressure increase on the upslope quite well. However, the magnitude of the pressure trough at the wave crest is under-predicted in both cases and some sensitivity to resolution is

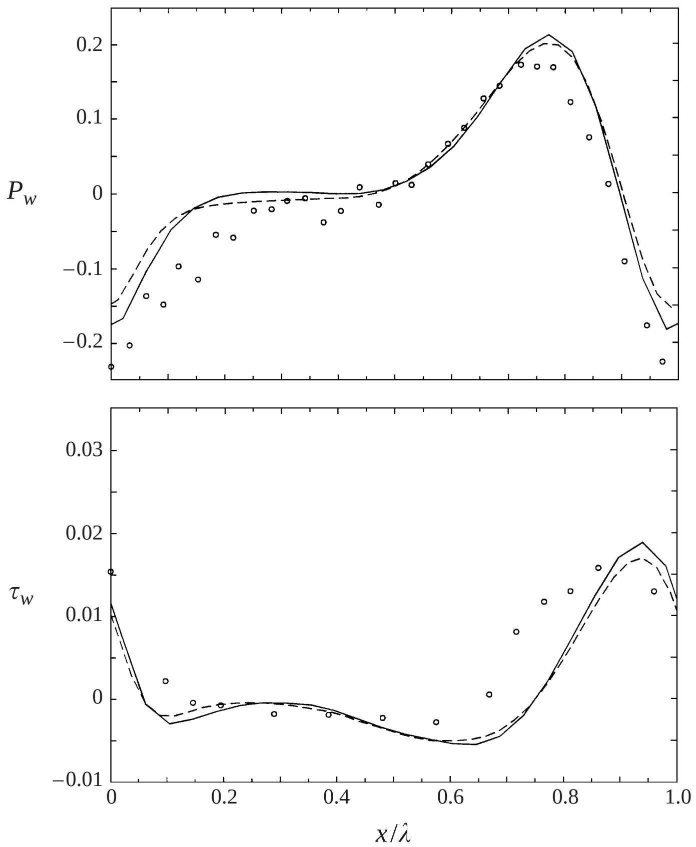

FIGURE 21. Non-dimensional wall pressure and surface shear stress distributions. ——, BHA1; — — —, BHA1R; symbols are data of BHA.

evident. The wall shear stress is generally well predicted although the phasing of the peak stress lags somewhat compared to the experiment. Note that the experimental surface shear stress was estimated by assuming a linear velocity profile from the lowest measurement point to the wall and there is some uncertainty associated with these measurements.

The total forces on the lower wall per unit area in the x-direction can be calculated by integrating the curves in figure 21. Defining the non-dimensional pressure and shear stress forces (per unit length) as

$$F_x = -\frac{2\pi a}{\lambda}\int_0^1 p_w\left(\frac{x}{\lambda}\right)\sin\left(2\pi\frac{x}{\lambda}\right)\mathrm{d}\left(\frac{x}{\lambda}\right), \tag{19}$$

$$T_x = \int_0^1 \tau_w\left(\frac{x}{\lambda}\right)\mathrm{d}\left(\frac{x}{\lambda}\right), \tag{20}$$

the experimental values are $F_x = 0.0261$ and $T_x = 0.0028$. This compares with $F_x = 0.0253$ and 0.0265 for BHA1 and BHA1R, respectively; the corresponding results for the shear stress are $T_x = 0.0016$ and 0.0014. The accurate prediction of the pressure force, commonly called the form drag, is due almost entirely to the fact that the pressure rise in figure 21 matches the data well. The under-prediction of the pressure trough is not critical to the integrated force in the x-direction since

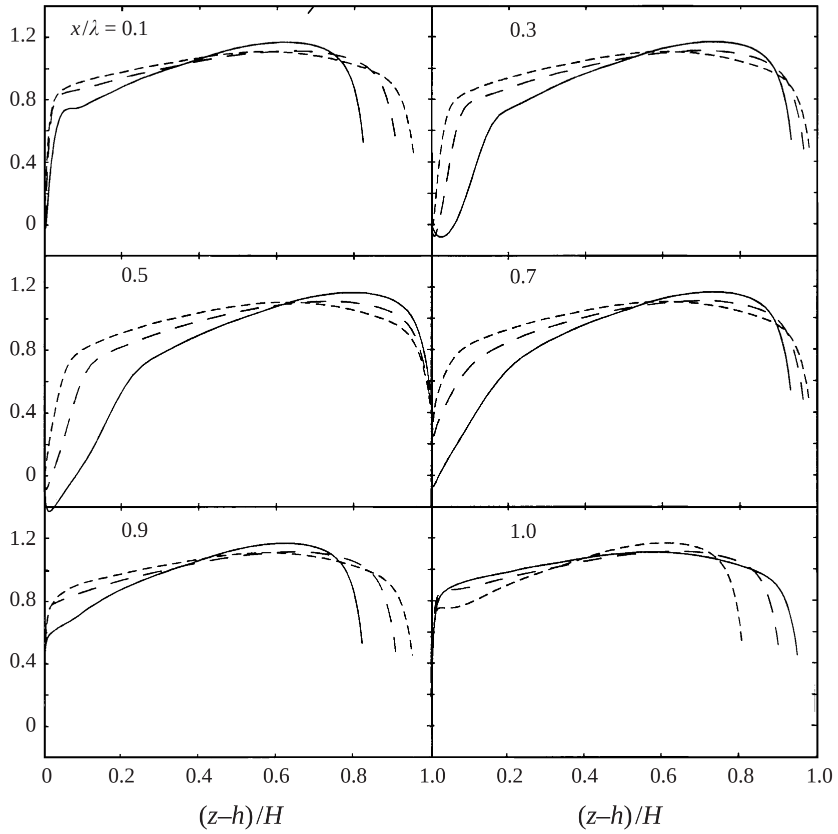

FIGURE 22. Profiles of mean streamwise velocity for 3 slopes: ——, case BHA1 ($2a/\lambda = 0.2$); – – –, case S3 ($2a/\lambda = 0.1$); – – –, case S2 ($2a/\lambda = 0.05$).

the local pressure force there acts vertically. However, the predicted shear stress force is significantly lower than the experimental observations because the biggest discrepancy occurs on the upslope (which is opposite to what we just noted for the pressure distribution). This discrepancy stems from an underprediction of the acceleration on the upslope and the resulting delayed flow reattachment. Although the difficulty in measuring velocity close to the surface may be a factor in the discrepancy, the magnitude of the shear stress component is small compared with the pressure contribution, so the total drag force is reasonably well predicted by the numerical simulation.

7. Variations with slope

The LES model has been used to examine the effects of varying wave slope. Figure 22 shows mean streamwise velocity profiles for $2a/\lambda = 0.05$, 0.10 and 0.20 (cases S2, S3 and BHA1 in table 1). It is evident that the mean flow separates for $2a/\lambda = 0.1$ but the 0.05 case is marginal in this regard. Other profile locations (not shown) between $x/\lambda = 0.3$ and 0.5 reveal that case S2 does show a very small region of flow separation. This finding is consistent with the flow regime map of Kuzan & Hanratty (1989), which also indicates that the higher slope cases will show clearly separated mean flow. The depth of the shear region above the trough clearly scales

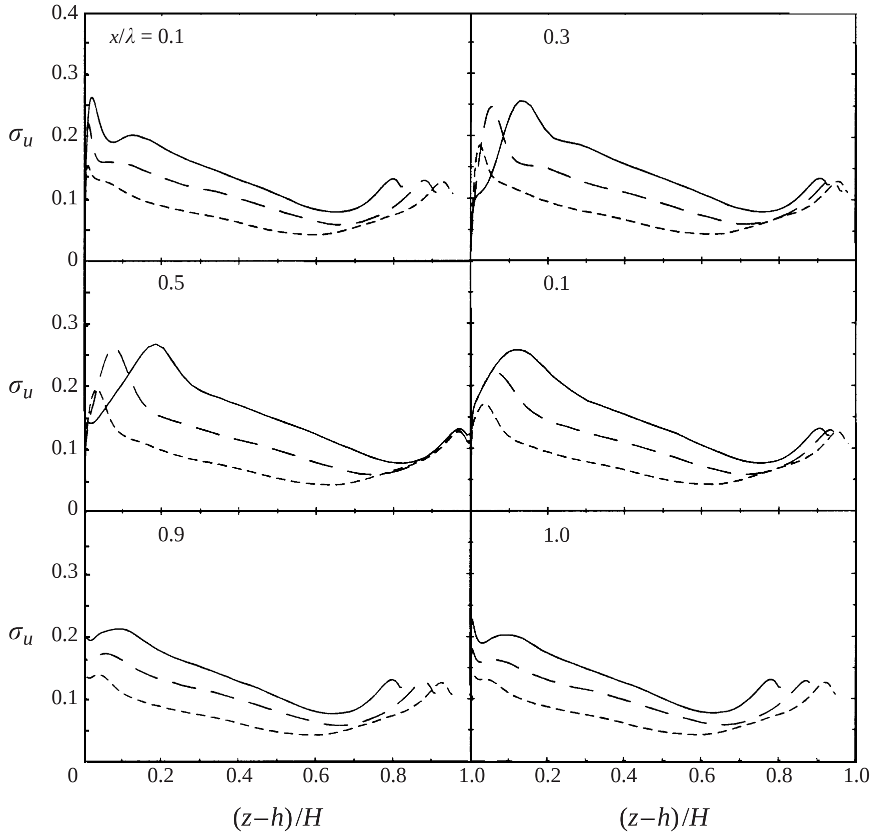

FIGURE 23. Profiles of mean streamwise turbulence intensity for cases BHA1, S3 and S2. Line patterns as in figure 22.

with the wave amplitude. This is also true for the height of maximum streamwise turbulence intensity, shown in figure 23. The turbulence intensity increases almost linearly with slope, especially away from the wave surface.

Figure 24 shows the variation in surface pressure and shear stress with wave slope. The pressure curves show a definite change in character as slope increases. The small-amplitude wave produces a smooth, slightly asymmetric, curve that is similar to the one shown in Zilker & Hanratty (1979) for this slope, but with a somewhat smaller peak. However, there may be some Reynolds-number effect given that the measurements by Zilker & Hanratty are for $Re = 30\,000$. As slope increases, a nearly constant pressure region over the separated flow becomes more pronounced. The shape of the $2a/\lambda = 0.2$ curve is similar to that in Zilker & Hanratty (as well as BHA), but apparently the LES significantly underpredicts the total pressure perturbation (peak-to-trough). (As we saw above, the $2a/\lambda = 0.2$ case shows good overall agreement with the data of BHA if the predictions and observations are matched in the region of uniform pressure at the trough.) A comparison of the $2a/\lambda = 0.1$ case with the $2a/\lambda = 0.125$ data in Zilker & Hanratty also reveals an underprediction of the pressure perturbation. In this case, though, the curves are also qualitatively different. As noted above, the LES curve shows evidence of separation by a relatively flat section. However, although Zilker & Hanratty observed separation at this slope, their pressure data do not show a similar feature.

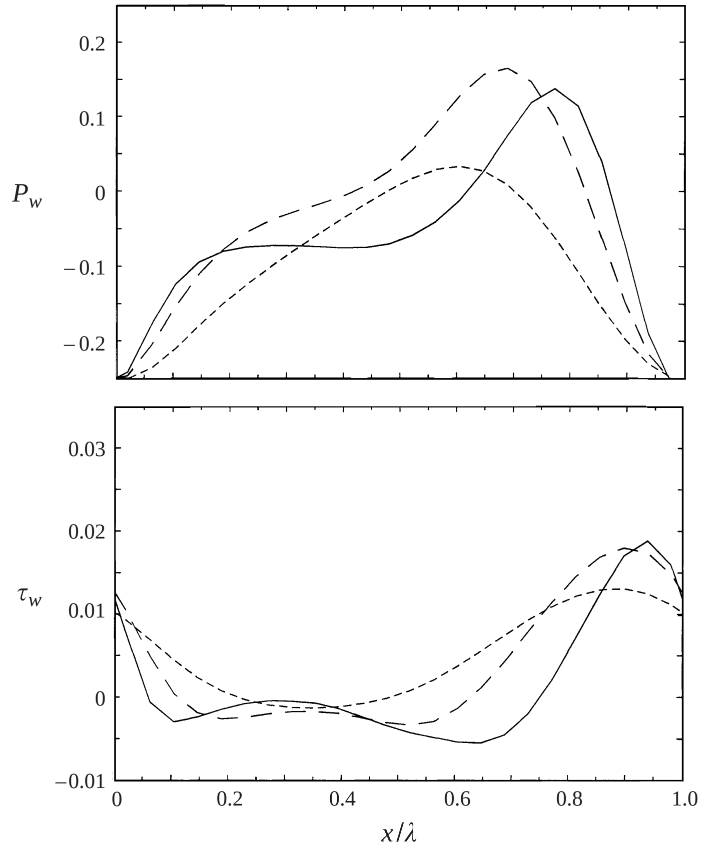

FIGURE 24. Non-dimensional wall pressure and surface shear stress distributions for cases BHA1, S3 and S2. Line patterns as in figure 22.

The surface shear stress curves shown in figure 24(*b*) clearly illustrate the regions of separated or stagnant flow for the three slopes. The shear stress for $2a/\lambda = 0.05$ is nearly symmetric (implying very little contribution to the increase in total surface force) and becomes slightly negative approximately from $x/\lambda = 0.2$ to 0.5. In light of the velocity profiles in figure 22, it is evident that the flow here is only weakly separated and is probably better characterized as stagnant. The region of negative shear stress clearly increases with slope, as does the magnitude of the negative stress. The local maximum that both $2a/\lambda = 0.1$ and 0.2 cases exhibit around $x/\lambda = 0.3$ is rather surprising, but results from a small reduction in the magnitude of the reverse flow there. Since measurements of surface shear stress are somewhat unreliable, we cannot ascertain if this feature is realistic. Because the reattachment point (the second zero stress crossing) moves downstream with increasing slope, the subsequent rate of increase in shear stress tends to be greater, although the location of the maximum also tends to move downstream slightly.

The pressure curves in figure 24(*a*) certainly show significant variations with slope. However, probably of greater interest than the curves themselves is the resulting integrated force on the wave surface, especially as a function of slope. This is examined in the next section.

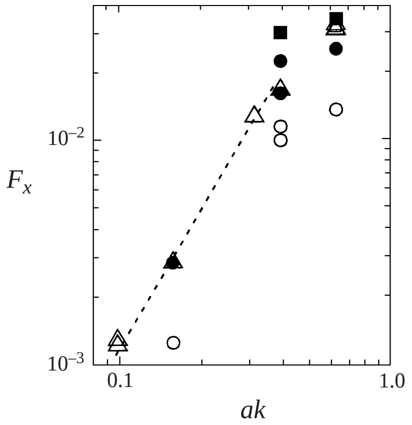

FIGURE 25. Form drag vs. wave slope as given in table 3: ○, data of Zilker & Hanratty (1979); ●, integration of Zilker & Hanratty pressure data; □, data of BHA; ■, integration of BHA pressure data; Δ, integration of LES surface pressure. Dashed line is proportional to $(ak)^2$.

8. Form drag calculations

In this section, we present LES calculations of form drag for a number of wave slopes; see table 1 for a summary of cases. These calculations include some variations with resolution and Reynolds number since the results may be somewhat controversial and we want to establish the sensitivity and consistency of the numerical calculations.

Figure 25 shows the variations in form drag as a function of slope. In comparing with the data of Zilker & Hanratty, as is done in Belcher *et al.* (1993) and Gong *et al.* (1996), we found that the LES form drag predictions were approximately twice as large as the reported values. However, we checked the Zilker & Hanratty results by integrating the corresponding pressure curves as presented in their paper. As seen from table 3, the numerically integrated forces are around twice the values stated in Zilker & Hanratty and are reasonably consistent with the LES results as well as the measurements of BHA. These calculations are shown in figure 25 as the solid symbols. We have employed this method on the data of BHA and obtain very close agreement with the reported form drag (within 6%). We also show the form drag derived from the pressure data presented in Buckles *et al.* (1986) for $2a/\lambda = 0.125$ ($Re = 12\,300$), although they do not give their own calculated value. The form drag in this case appears to be quite high, being roughly equal to the value for $2a/\lambda = 0.2$, although not that much higher than the numerically integrated Zilker & Hanratty result for $Re = 14\,730$. This suggests there may be some dramatic change in the nature of the flow at this slope, possibly with some Reynolds-number dependence, or it may point out some difficulties and uncertainties in the measurements. Note that the measurements of Gong *et al.* are still in reasonable agreement with the adjusted values of Zilker & Hanratty, particularly if the normalization in Gong *et al.* is corrected for the fact that the centreline velocity is approximately 20% larger than the bulk velocity. However, the predictions in Belcher *et al.* appear to be much lower than the adjusted Zilker & Hanratty forces as well as those of BHA and the LES in this study.

We have examined sensitivity to resolution, domain length and Reynolds number for $2a/\lambda = 0.2$. As can be seen from the figure and table 3, the form drag calculated from the LES appears to be relatively insensitive in the range of Reynolds numbers

Reference	$2a/\lambda$	Re	F_x	$\lambda^{-1}\int_0^\lambda p_w \frac{\mathrm{d}h}{\mathrm{d}x}\mathrm{d}x'$
Zilker & Hanratty (1979)	0.05	29 300	1.26×10^{-3}	2.89×10^{-3}
	0.125	14 730	1.155×10^{-2}	2.29×10^{-2}
	0.125	30 000	1.003×10^{-2}	1.64×10^{-2}
	0.20	30 530	1.37×10^{-2}	2.56×10^{-2}
Buckles *et al.* (1986)	0.125	12 300	—	3.08×10^{-2}
BHA	0.20	10 700	3.27×10^{-2}	3.46×10^{-2}
LES-S1	0.031	6560	—	1.24×10^{-3}
S1R	0.031	5720	—	1.31×10^{-3}
S2	0.05	11 050	—	2.90×10^{-3}
S3	0.10	10 580	—	1.29×10^{-2}
S4	0.125	10 800	—	1.70×10^{-2}
BHA1	0.20	10 600	—	3.16×10^{-2}
BHA1R	0.20	10 450	—	3.34×10^{-2}
BHA1L	0.20	12 000	—	3.21×10^{-2}
BHA2	0.20	5990	—	3.20×10^{-2}
BHA3	0.20	20 060	—	3.19×10^{-2}

TABLE 3. Form drag for various wave slopes and Reynolds numbers. F_x is the normalized form drag given in the cited references; the last column is the form drag computed using published surface pressure data (calculated by the present authors). Note that the values for BHA and Buckles *et al.* (1986) are scaled by $(H-a)^2/(H-2a)^2$ so they are consistent with U_b defined by (17).

considered. This is in contrast to Zilker & Hanratty, especially for the numerically integrated pressure forces, although there is certainly some question as to the reliability of these force results.

It should be pointed out that the LES results are subject to some uncertainty since they depend entirely on modelling the flow near the surface where, as has been shown, the explicit resolution of the turbulent motions is effectively reduced. However, the effective resolution increases with slope since larger-scale motions are generated and the form drag predictions are self-consistent in that a quadratic dependence on slope is shown over a range of amplitudes, i.e. a good fit is given by

$$F_x = 0.12(ak)^2.$$

This relationship appears to be valid up to around $2a/\lambda = 0.1$; it starts to fall off as slope and hence separation increases. This behaviour is consistent with theoretical expectations, e.g. Wood & Mason (1993).

9. Increased transverse fluctuations

As shown in figure 18, the transverse fluctuations, $\overline{v'^2}$, show a marked increase on the upslope close to the wave surface. In fact, the largest velocity fluctuations are found in the lateral component, exceeding even the streamwise component maximum, located in the separating shear layer. A similar feature has recently been reported by De Angelis *et al.* (1997) and Cherukat *et al.* (1998) in their DNS studies of flow over waves with smaller slopes, although not as pronounced as in figure 18. The magnitude and limited spatial extent of the $\overline{v'^2}$ increase strongly suggests a localized energy production mechanism associated with the wave slope and we, therefore, investigate the lateral velocity fluctuations in more detail.

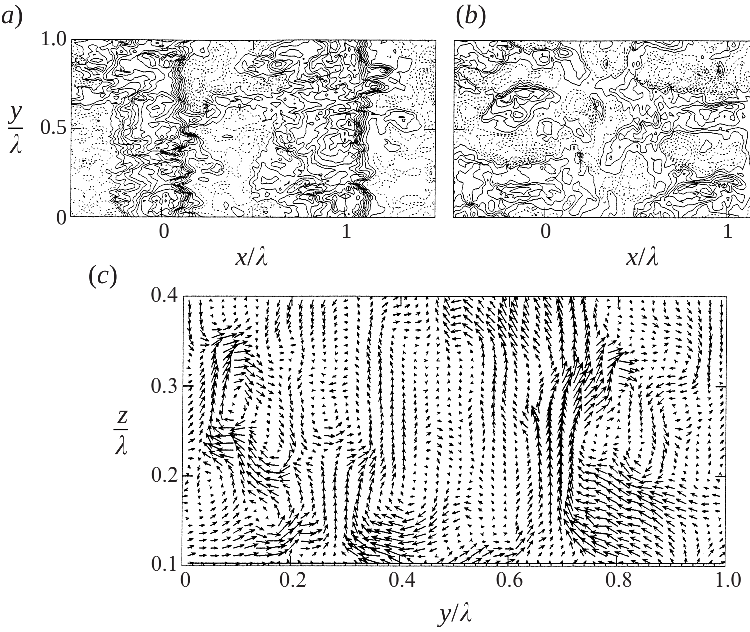

FIGURE 26. Instantaneous velocity fields from BHA1R. (*a*) *u*-component and (*b*) *v*-component at $\eta/\lambda = 0.025$. Contour interval is 0.1; dashed lines indicate negative values. (*c*) Secondary flow at $x/\lambda = 0.75$. The vectors are interpolated onto a 48×36 uniform grid. The maximum velocity is 0.7.

An examination of instantaneous flow fields at $\eta/\lambda = 0.025$, such as that shown in figure 26, indicates structures elongated in the streamwise direction; they are most easily seen in the transverse velocity field. However, they do not resemble the streaks seen in flat boundary layers: these are broader laterally and limited in streamwise extent. These broad areas of coherent transverse velocity are also evident in a plot of the secondary flow vectors at $x/\lambda = 0.75$, figure 26(*c*). There are intense vortex-like transverse motions close to the surface, but they do not seem to be clearly defined closed circulations or streamwise rolls.

The velocity fluctuations associated with these intense transverse velocity regions are strongly affected by the presence of the solid boundary, since they occur so close to the wall. This is most probably the reason for the preferential manifestation of the kinetic energy in the *v*-component, rather than equally amongst *v* and *w*. For a streamwise vortex, an idealized reflective boundary condition at the wall reduces the normal component of the velocity to zero and doubles the transverse velocity component, giving strong enhancement of $\overline{v'^2}$ at the surface. The wall layer drag reduces the velocity very close to the surface, but the large increase in $\overline{v'^2}$ on the lower side of the vortex-like structures is clearly evident in the LES results.

The persistence of these structures is illustrated in figure 27, which shows the transverse velocity component at $x/\lambda = 0.75$ and $\eta/\lambda = 0.0125$ as a function of time and transverse position. Examples from BHA1 and the flat channel case F are shown. It can be seen that the flat channel contours are rather isotropic in appearance, indicating an intermittent flow structure that is not strongly correlated in time or along the transverse direction. In contrast, the contours for the wavy channel midway on the upslope show broad streaks of positive or negative velocity. Although these features meander laterally and the magnitude of the *v*-velocity in the streak is

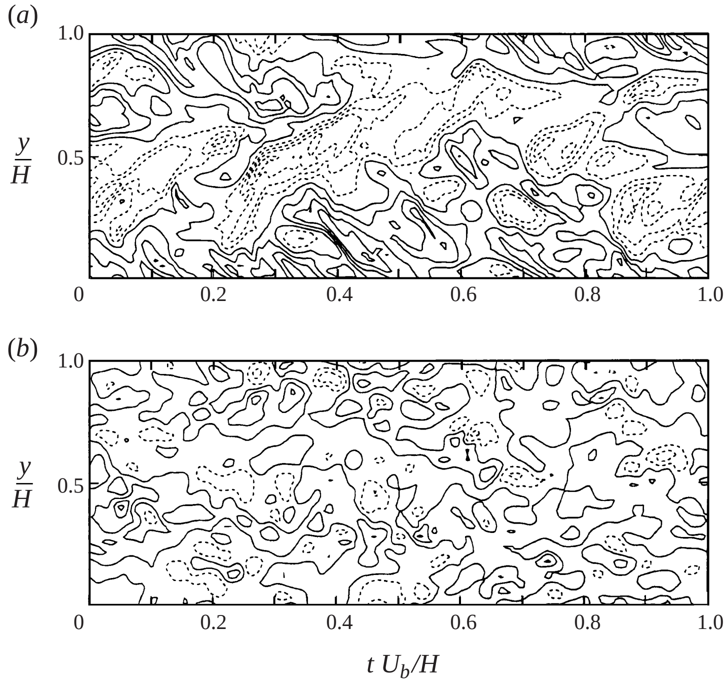

FIGURE 27. Transverse velocity at fixed streamwise and vertical position as a function of lateral position and time; (*a*) BHA1 at $x/\lambda = 0.75$ and $\eta/\lambda = 0.0125$, contour intervals are 0.1. (*b*) Case F at $z/H = 0.01$, contour intervals are 0.05.

modulated over time, the identity of the structure is maintained throughout, providing strong evidence of their stability.

Both De Angelis *et al.* (1997) and Cherukat *et al.* (1998) suggest that the transverse velocity fluctuation increase is produced by the large-scale structures associated with flow separation and reattachment. This is not necessarily the case. Although the $\overline{v'^2}$ maximum is localized near the reattachment point over the large-amplitude wave, LES of flow over smaller wave slopes also show a similar feature on the wave upslope. Figure 28 shows the transverse fluctuation intensities for the three waves considered in §8. Note that the maximum on the upslope is present for all waves, including the smallest slope that exhibits very weak separation. (The mean reattachment point in that case is at $x/\lambda = 0.5$, well upstream of the $\overline{v'^2}$ maximum.)

Figure 29 shows the transverse variance perturbation for case S1R, as was done for the streamwise and vertical components in figure 10. It can be seen that for a small-amplitude wave, a noticeable increase in $\Delta\overline{v'^2}$ on the upslope is evident, but it is accompanied by an almost equal decrease on the downslope. (However, an examination of the larger-amplitude waves reveals that this near anti-symmetry breaks down as slope increases so that the magnitude of the upslope (positive) perturbation becomes much larger than the magnitude of the downslope (negative) perturbation.) In contrast to figure 10, there is little qualitative agreement with closure model predictions.

The perturbation maximum in figure 29 is close to the surface and thus is influenced by the subgrid model, but figure 11 shows that at least 75% of the transverse variance is resolved at that location. Also, the fraction of resolved variance increases with slope (not shown), so results should be more reliable for the larger-amplitude cases.

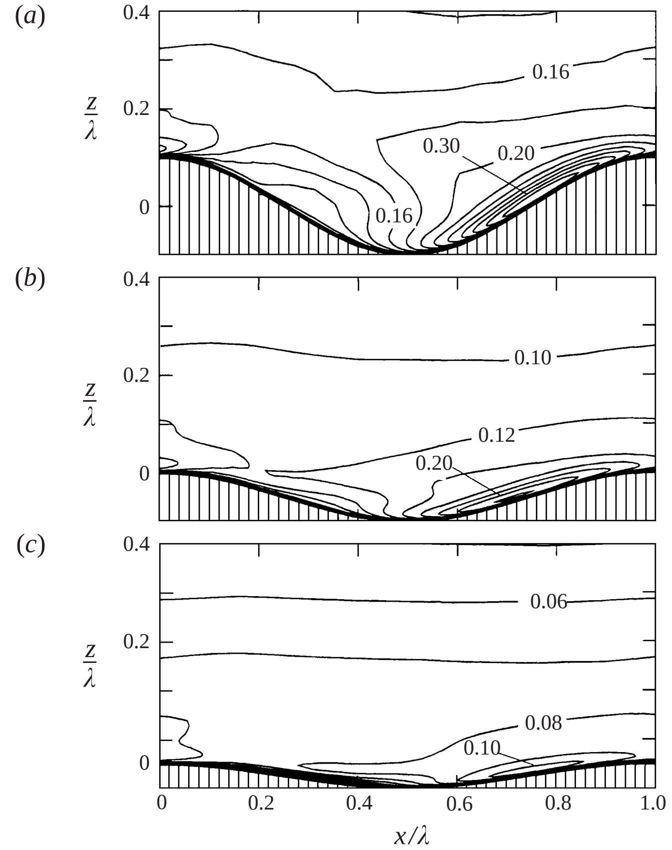

FIGURE 28. Transverse fluctuation intensity, σ_v, for three wave slopes. (*a*) BHA1, (*b*) S3, (*c*) S2.

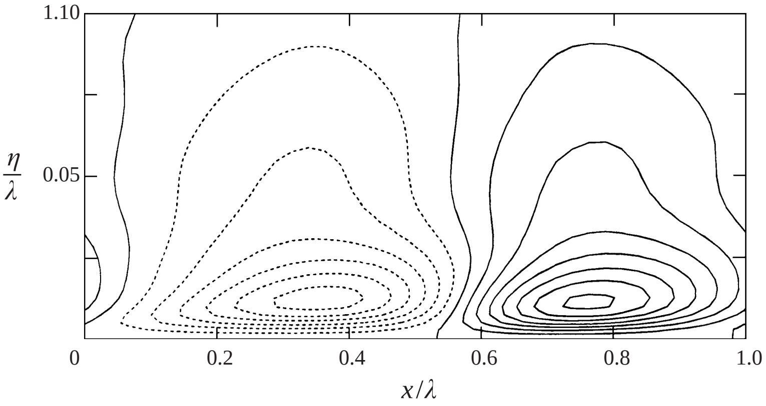

FIGURE 29. Transverse velocity variance perturbation from the wavelength average, normalized by u_*^2, for case S1R. Contour interval is 0.1. Dashed lines indicate negative values.

The results shown in figure 28 indicate that $\overline{v'^2}$ increases with wave steepness. To quantify this, we examine the normalized maximum perturbations for the streamwise and transverse variances as functions of wave slope, given in table 4. In can be seen that $\Delta\overline{u'^2}$ scales closely with slope for small-amplitude waves, in accord with linear

LES case	ak	$\Delta\overline{u'^2}/ak$	$\Delta\overline{v'^2}/(ak)^2$
S1	0.098	7.70×10^{-2}	2.41×10^{-1}
S1R	0.098	8.43×10^{-2}	2.50×10^{-1}
S2	0.157	7.91×10^{-2}	1.93×10^{-1}
S3	0.314	9.13×10^{-2}	2.64×10^{-1}
S4	0.393	8.18×10^{-2}	1.86×10^{-1}
BHA1	0.628	8.67×10^{-2}	1.69×10^{-1}
BHA1R	0.628	6.47×10^{-2}	1.34×10^{-1}
BHA1L	0.628	9.55×10^{-2}	1.81×10^{-1}

TABLE 4. Maximum variance perturbations for LES cases defined in table 1. The streamwise perturbations are normalized by the wave slope ak; the transverse perturbations are normalized by the square of the wave slope.

theories (Sykes 1980). However, the $\Delta\overline{v'^2}$ increases suggest a quadratic dependence on slope, with a fall off at larger slopes similar to the form drag.

Examination of the conservation equation for $\overline{v'^2}$ shows that, since there are no mean gradients in the lateral direction, direct production terms are zero and the transverse velocity fluctuations must be driven by the pressure-strain term, $\overline{p'\partial v'/\partial y}$, as pointed out by De Angelis *et al.* (1997). It is well-known that pressure-strain terms redistribute energy from one component to another and this is clearly the case with $\overline{v'^2}$; energy from the streamwise and/or vertical components is extracted through the correlation between pressure perturbations and transverse velocity gradients. The proximity of the wall is certainly a factor, as mentioned above, but the basic mechanism that gives rise to this correlation is unknown. It may be due to amplification of some flow instability, but it is not related to the large-scale shear instability described in Phillips, Wu & Lumley (1996) and possibly observed in the experiments of Gong *et al.* (1996), since that mechanism has a streamwise scale greater than the wavelength. The increased $\overline{v'^2}$ we observe is much more limited in extent. A possible mechanism is the Taylor–Görtler instability which produces streamwise vortices such as observed in boundary-layer flow over a concave surface (e.g. Tani 1962; So & Mellor 1975; Hoffman, Muck & Bradshaw 1985). The trough region presents a concave surface, and we might therefore expect production of coherent streamwise vortices in the local flow. However, the magnitude of the $\overline{v'^2}$ increase observed in the LES calculations appears to be significantly larger than experimental observations in curved boundary-layer flow, but this may be due to enhancement by the shear distortion in the flow over the waves. Experimental flows have generally involved minimal streamwise acceleration in an attempt to isolate the curvature mechanisms. In contrast, the vorticity production in flow over waves occurs in a region of strong acceleration and, hence, vortex stretching. Streamwise vorticity is therefore enhanced as the flow accelerates toward the wave crest, increasing the v-velocity and also stabilizing any existing vortices.

10. Conclusions

Large-eddy simulations of flow over a wavy surface have been presented and compared with available experimental data at Reynolds numbers of about 10^4. The viscous effects are only important close to the smooth wall, and the LES grid size normal to the wall is chosen to resolve the viscous sublayer. A range of wave amplitudes has been studied, from small slopes with almost linear flow perturbations up to steep waves with large-scale flow separation. Particular attention has been paid to the large-amplitude wave experiment of BHA.

In spite of the fact that surface elevation variations are known to induce complex distortion of the turbulence fields close to the surface, the moderate resolution of the LES appears sufficient to capture many aspects of the experimental flow. This is partially due to the fact that the streamwise velocity fluctuations, often the only component measured in the laboratory, are relatively well resolved in the LES. Nevertheless, the response of the mean flow and the streamwise velocity variance to different wave amplitudes is accurately predicted even close to the surface.

Small-amplitude waves illustrate the nature of the perturbations, and confirm the turbulence closure model predictions of an 'inner layer' structure between the wall-layer and the outer flow on the scale of the horizontal wavelength. The LES results show rapid variations in the velocity variances within a layer of about 5% of the wavelength; this is generally consistent with closure theory predictions but quantitative comparison is precluded by the log-layer assumption of the analytical models.

At large amplitude, the flow is dominated by the separating shear layer which generates large-scale eddies, allowing more of the turbulent energy to be resolved by the LES. The predicted separation region is more extensive than in the experiment, but the turbulent and mean flow fields are only sensitive to this discrepancy very close to the wall. The predicted structure of the streamwise velocity fluctuations, including the higher-order statistics of skewness and flatness, is consistent with the experimental data.

A comparison of predicted form drag with experimental observations has pointed out some uncertainties in the observations. In particular, in appears that the drag coefficients reported in Zilker & Hanratty (1979) are inconsistent with their surface pressure distributions. However, the form drag reported in BHA (which is consistent with their surface pressure data) is close to the LES value. The LES results are subject to uncertainty since resolution is effectively reduced near the surface, but they are self-consistent in that the form drag shows a quadratic dependence on slope for small-amplitude waves, as predicted by analytical models. A slight fall off with slope is predicted for larger amplitudes, again consistent with expectations (e.g. Wood & Mason 1993).

One of the most striking features of the numerical calculation is a dramatic increase in lateral velocity variance in a very localized region close to the surface on the upslope of the wave. This is a general feature of all our wavy surface simulations. The increase apparently scales with the square of the slope, in contrast to the other two velocity components, which scale linearly with slope for small-amplitude waves. The eddies responsible for the high variance are persistent structures, elongated along the upslope, with relatively large lateral scale. The lateral motions are driven by pressure variations, constrained by the tangential plane of the wall, but the basic mechanism for their generation is unclear. This phenomenon has been observed in the DNS studies of De Angelis *et al.* (1997) and Cherukat *et al.* (1998), but, as far as we are aware, not measured experimentally, and further investigation is warranted.

This work was supported by the US Army Research Office under contract DAAH04-95-G-0041, monitored by Walter J. Bach, Jr.

REFERENCES

Belcher, S. E. & Hunt, J. C. R. 1998 Turbulent flow over hills and waves. *Ann. Rev. Fluid Mech.* **30**, 507–538.

Belcher, S. E., Newley, T. M. J. & Hunt, J. C. R. 1993 The drag on an undulating surface induced by the flow of a turbulent boundary layer. *J. Fluid Mech.* **249**, 557–596.

Buckles, J. J. 1983 Turbulent separated flow over wavy surfaces. PhD thesis, University of Illinois.

Buckles, J., Hanratty, T. J. & Adrian, R. J. 1984 Turbulent flow over large-amplitude wavy surfaces. *J. Fluid Mech.* **140**, 27–44.

Buckles, J., Hanratty, T. J. & Adrian, R. J. 1986 Separated turbulent flow over a small amplitude wave. *Laser Anemometry in Fluid Mechanics – II* (ed. R. J. Adrian, D. F. G. Durao, F. Durst, H. Mishina & J. H. Whitelaw), pp. 347–357. Ladoan, Lisbon.

Cherukat, P., Na, Y., Hanratty, T. J. & McLaughlin, J. B. 1998 Direct numerical simulation of a fully developed turbulent flow over a wavy wall. *Theoret. Comput. Fluid Dyn.* **11**, 109–134.

Clark, J. A. 1968 A study of incompressible turbulent boundary layers in channel flow. *Trans. ASME* D: *J. Basic Engng* **90**, 455–467.

Clark, T. L. 1977 A small-scale dynamic model using a terrain-following coordinate transformation. *J. Comput. Phys.* **24**, 186–215.

De Angelis, V., Lombardi, P. & Banerjee, S. 1997 Direct numerical simulation of turbulent flow over a wavy wall. *Phys. Fluids* **9**, 2429–2442.

Dörnbrack, A. & Schumann, U. 1993 Numerical simulation of turbulent convective flow over wavy terrain. *Boundary-Layer Met.* **65**, 323–355.

Frederick, K. A. 1986 Turbulent air flow over hills. PhD thesis, University of Illinois.

Frederick, K. A. & Hanratty, T. J. 1988 Velocity measurements for a turbulent nonseparated flow over solid waves. *Exps Fluids* **6**, 477–486.

Gong, W., Taylor, P. A. & Dörnbrack, A. 1996 Turbulent boundary-layer flow over fixed aerodynamically rough two-dimensional sinusoidal waves. *J. Fluid Mech.* **312**, 1–37.

Henn, D. S. & Sykes, R. I. 1992 Large-eddy simulation of dispersion in the convective boundary layer. *Atmos. Env.* **26**A, 3145–3159.

Hoffman, P. H., Muck, K. C. & Bradshaw, P. 1985 The effect of concave surface curvature on turbulent boundary layers. *J. Fluid Mech.* **161**, 371–403.

Hudson, J. D. 1993 The effect of a wavy boundary on a turbulent flow. PhD thesis, University of Illinois.

Hudson, J. D., Dykhno, L. & Hanratty, T. J. 1996 Turbulence production in flow over a wavy wall. *Exps Fluids* **20**, 257–265.

Hunt, J. C. R., Leibovich, S. & Richards, K. J. 1988 Turbulent shear flow over low hills. *Q. J. R. Met. Soc.* **114**, 1435–1470.

Hussain, A. K. M. F. & Reynolds, W. C. 1970 The mechanics of an organized wave in turbulent shear flow. *J. Fluid Mech.* **41**, 241–258.

Hussain, A. K. M. F. & Reynolds, W. C. 1975 Measurements in fully developed turbulent channel flow. *Trans. ASME* D: *J. Fluids Engng* **97**, 568–578.

Krettenauer, K. & Schumann, U. 1992 Numerical solution of turbulent convection over wavy terrain. *J. Fluid Mech.* **237**, 261–300.

Kuzan, J. D., Hanratty, T. J. & Adrian, R. J. 1989 Turbulent flows with incipient separation over solid waves. *Exps Fluids* **7**, 88–98.

Lewellen, W. S. 1977 Use of invariant modeling. *Handbook of Turbulence* (ed. W. Frost & T. H. Moulden), pp. 237–280. Plenum Press.

Maaß, C. & Schumann, U. 1994 Numerical simulation of turbulent flow over a wavy boundary. *Direct and Large Eddy Simulation – I* (ed. P. R. Voke, L. Kleiser & J. P. Chollet), pp. 287–297. Kluwer.

Maaß C. & Schumann, U. 1996 Direct numerical simulation of separated turbulent flow over a wavy boundary. *Flow Simulation with Higher Performance Computers – II* (ed. E. H. Hirschel), pp. 227–241.

Mason, P. J. 1989 Large-eddy simulation of the convective atmospheric boundary layer. *J. Atmos. Sci.* **46**, 1492–1516.

Mason, P. J. & Callen, N. S. 1986 On the magnitude of the subgrid-scale eddy coefficient in large-eddy simulations of turbulent channel flow. *J. Fluid Mech.* **162**, 439–462.

Moin, P. & Kim, J. 1982 Numerical investigation of turbulent channel flow. *J. Fluid Mech.* **118**, 341–377.

Newley, T. M. J. 1985 Turbulent air flow over hills. PhD thesis, Cambridge University.

Phillips, W. R., Wu, Z. & Tumley, J. L. 1996 On the formation of longitudinal vortices in a turbulent boundary layer over wavy terrain. *J. Fluid Mech.* **326**, 321–341.

Schmidt, H. & Schumann, U. 1989 Coherent structure of the convective boundary layer derived from large-eddy simulations. *J. Fluid Mech.* **200**, 511–562.

So, R. M. C. & Mellor, G. L. 1975 Experiment on turbulent boundary layers on a concave wall. *Aero. Q.* **26**, 25–40.

Sykes, R. I. 1980 An asymptotic theory of incompressible turbulent boundary-layer flow over a small hump. *J. Fluid Mech.* **101**, 647–670.

Sykes, R. I. & Henn, D. S. 1989 Large-eddy simulation of turbulent sheared convection. *J. Atmos. Sci.* **46**, 1106–1118.

Sykes, R. I. & Henn, D. S. 1992 Large-eddy simulation of concentration fluctuations in a dispersing plume. *Atmos. Env.* **26**A, 3127–3144.

Tani, I. 1962 Production of longitudinal vortices in the boundary layer along a concave wall. *J. Geophys. Res.* **67**, 3075–3080.

Taylor, P. A. 1977 Numerical studies of neutrally stratified planetary boundary-layer flow above gentle topography. *Boundary-Layer Met.* **12**, 37–60.

Walko, R. L., Cotton, W. R. & Pielke, R. A. 1992 Large-eddy simulations of the effects of hilly terrain on the convective boundary layer. *Boundary-Layer Met.* **58**, 133–150.

Wood, N. & Mason, P. J. 1993 The pressure force induced by neutral, turbulent flow over hills. *Q. J. R. Met. Soc.* **119**, 1233–1267.

Zilker, D. P. 1976 Flow over wavy surfaces. PhD thesis, University of Illinois.

Zilker, D. P., Cook, G. W. & Hanratty, T. J. 1977 Influence of the amplitude of a solid wavy wall on a turbulent flow. Part 1. Non-separated flows. *J. Fluid Mech.* **82**, 29–51.

Zilker, D. P. & Hanratty, T. J. 1979 Influence of the amplitude of a solid wavy wall on a turbulent flow. Part 2. Separated flows. *J. Fluid Mech.* **90**, 257–271.